Kinematics, Dynamics and Control of Single-Axle, Two-Wheel Vehicles (Biplanar Bicycles)

Michael Shawn Abbott

Thesis submitted to the Faculty of the
Virginia Polytechnic Institute and State University
in partial fulfillment of the requirements for the degree of

MASTER OF SCIENCE

in

Mechanical Engineering

APPROVED:

C. F. Reinholtz, Chair
H. H. Robertshaw
D.J. Leo

April 11, 2000
Blacksburg, Virginia

Key Words: Dynamics, Control, Two-Wheel, Vehicle

Kinematics, Dynamics and Control of Single-Axle, Two-Wheel Vehicles (Biplanar Bicycles)

Michael Shawn Abbott

Charles F. Reinholtz, Chairman

Mechanical Engineering

(ABSTRACT)

A two-wheeled, single-axle, differentially driven vehicle possesses many salient advantages when compared to traditional vehicle designs. In particular, high traction factor, zero turn radius, and inherent static and dynamic stability are characteristics of this configuration. Drive torque is provided via a swinging reaction mass hanging below the axle. While mechanically simple, the resulting nonlinear vehicle dynamics can be quite complex. Additional design challenges arise if non-pendulating platforms or hardware mounts are required. Ultimately, this vehicle class has great potential in autonomous robotic applications such as mine clearance, planetary exploration, and autonomous remote inspection. This thesis discusses the kinematic and dynamic analyses of this vehicle class and develops design tools including performance envelopes and control strategies. Further, it confronts the stable platform problem and provides one solution while suggesting alternative design concepts for other applications.

Acknowledgements

Many people have contributed to this work and have made it possible for me to escape with what little sanity remains. I would like to thank Dr. Charles F. Reinholtz, my advisor for the duration, for supporting me during my time here at Virginia Tech. He has provided direction and opinion grounded in the reality that I all too often allow to pass by the wayside in my quest for solutions. He has also been a friend and mentor and I sincerely hope we find opportunities in the future to work together once again. I would also like to extend my thanks to Dr. Harry Robertshaw, the man who has taught me the importance of written and oral communication skills in the engineering profession. Further, his outlook on life has been inspiring and at times, frightening. He, above all, exemplifies the importance maintaining a realistic opinion of the importance of your work; it keeps you honest. Dr. Leo must also be mentioned for his contribution to my overall graduate experience. He filled in the sometimes-overlooked gap between understanding a dynamic system and being able to control its actions.

Anyone who was around when I began my graduate career knows that I have to thank Randy Soper: colleague, mentor, sounding board, and friend. He single-handedly convinced me to take intermediate dynamics which, while draining me of every last ounce of energy and motivation, opened an entirely new world of engineering in which I have been playing ever since. Although we never published our world-shattering theories

mulled over while eating free chips and taco salads, the intellectual stimulation drove me further than I ever thought I could go. Finally, he was responsible for getting me started on this work in the first place.

Above anyone else I would like to thank Heather Kennedy, the most important person in my life. I am forever grateful that she put up with me during the times I spent nearly one hundred hours a week at the office (again, probably Randy's fault). Her patience in understanding that my stench of gear oil and axle grease was a necessary evil if my sanity was to remain during the few hours I was not in the office. She has been a tremendous emotional and psychological support to me throughout these past few years and for that I am eternally thankful.

Finally, I'd like to send an olé to all those folks that have kept the office so well fed.

Table of Contents

List of Figures

Chapter 1

Introduction

Since the inception of the wheel as a viable means of ground transportation, man has been on a never-ending quest to optimize its use for the transport of people and cargo. Vehicles of all shapes, sizes, and weights have been built to accomplish one task or another. Although vastly different in design and intended application, we could classify most ground vehicle in terms of a single design feature; the number of wheels. This classification does not predicate advantages of one vehicle over another. However, it does provide a metric against which the designer may estimate of a vehicle's potential performance characteristics and general capabilities. Therefore, it stands to reason that the historical record should demonstrate mankind's quest to classify the dynamic characteristics and performance advantages of vehicles with every conceivable number of wheels. This is in fact the case. Simply by examining the design and use of ground transportation throughout history, we can see both experimentation and refinement in the design of everything from vehicles having no wheels (tracks or legs) to those containing hundreds of wheels (trains). Figure 1.1 presents the best known single-wheel vehicle, the unicycle. Although this would have been the only possible configuration at the moment of the wheel's inception, the design has never proven itself as an effective means in the

transportation of people and cargo. However, it remains in mainstream society as a source of entertainment and amusement.

Figure 1.1: One-Wheel Vehicle

Figure 1.2: Standard Two-Wheel Vehicle

Likewise, we see in figure 1.2 the common perception of the two-wheel vehicle, the bicycle. This design, though inherently unstable, has found widespread use and acceptance throughout the world. Although the standard bicycle has met with great success in both human and engine-powered transportation its overall utility as a workhorse remains a point of debate. Millions of people all over the world rely on the standard bicycle as their primary mode of transportation. However, cargo capacity is meager at best.

At this point, we could make a strong argument for the correlation between how many wheels are on a vehicle and its relative usefulness to society. Indeed, we could continue this pattern by examining some of the more successful three-wheel designs. Though not as prevalent in number as bicycles and motorcycles, this design shows up in everything from toy tricycles to commercially successful off and on-road vehicles. Figure 1.3 presents a very successful three-wheel car marketed by the Morgan motor company during the late 1920's. Even though the design lost favor compared to vehicles with more wheels, these types of vehicles are still highly acclaimed and sought after by both collectors and driving enthusiasts. Naturally, they also tend to be much more stable than bicycles and motorcycles, but problems still exist. In fact, it was the high-speed

instability of the three-wheel all-terrain vehicle that ultimately led to its demise [Johnson, 1991]. So if we continue on the premise that more is better, we may consider several more steps in ground vehicle design.

Figure 1.3: Production Three-Wheel Vehicle (1929 Morgan Super Sports Aero)

Figure 1.4: Production Four-Wheel Vehicle (1963 Austin Healey 3000 MKII)

Nothing need be said concerning the success of the four-wheel vehicle; one of the finest examples of which is presented in figure 1.4. No other vehicle type has met with more public enthusiasm than the standard automobile. Four wheeled vehicles are used in public, private, and industrial transportation and have become an icon of the American dream. Again we see ever-increasing numbers of people and amounts of cargo being

moved over the world's roadways every year. Compared to the success of the four-wheel vehicle class, the popular two-wheelers and nearly forgotten three-wheelers are primitive in their capabilities. However, even with the incredible success of the four-wheelers, increasing utility does not end there. Larger trucks designed specifically for cargo handling can have anywhere from 10 to 22 wheels. These examples effectively support the thesis that more wheels inherently lead to more utility when considering the transportation of people and cargo.

Finally, if we take the utility to number of wheels correlation toward the limit, we find one of the most influential vehicle types since the development of the wheel itself, the train (Figure 1.5). Largely responsible for United States expansion in the West, the train represents to limit of the wheel-utility correlation. Most of a train's volume is dedicated to cargo. Its efficiency in ground transport is therefore undeniable. Even today when most Americans do not travel by train, it remains at the forefront of industrial transportation.

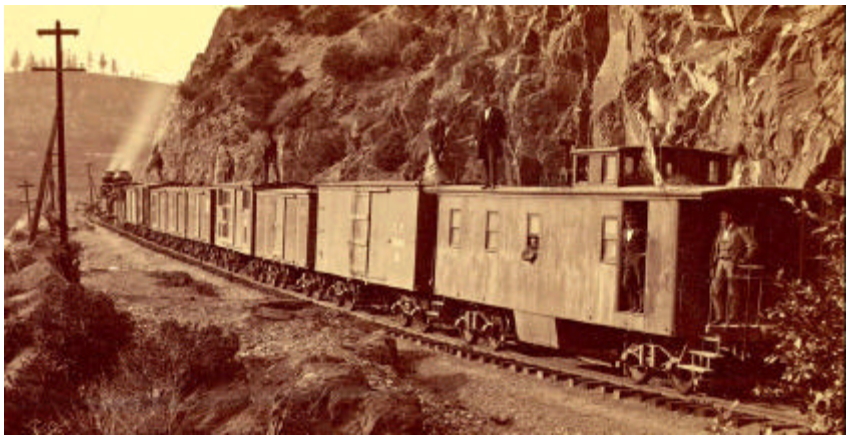

Figure 1.5: Multiple-Wheel ground vehicle: The Train

We have made an argument supporting the idea that more wheels are better. In light of this apparent correlation, one would assume that investigation of the two-wheel concept would prove fruitless. However, what must be considered here is that the historical development of ground vehicles has focussed on efficiency in business, commerce, and personal transportation. Further, designers of ground vehicles have in general worked

under the assumption that vehicle control would ultimately fall into the hands of a human pilot. If another metric of utility is employed, we see much different results.

Consider the case in which the motivating force for vehicular design is that of movement through harsh and discontinuous terrain as would be expected in cases such as warfare. Vehicles with multiple wheels are used for troop and cargo over prepared road surfaces but tracked vehicles have by far been the design class of choice for traversing off-road terrain. Further, tracked vehicles have proven effective in other conditions where the terrain is not groomed or conditioned for use with wheels. Planetary exploration, traversal of snow, and any application requiring a zero turn radius have been particularly attractive for this design concept. Clearly, some applications warrant a considerably different design approach than the one by which ground transportation has traditional been motivated.

Vehicular design for transport has evolved from focussing on the refinement of mechanics and suspension to focussing more on the integration of electronics and control systems. Therefore, most work in vehicular mechanical design is being done for non-traditional applications such as planetary exploration, traversal of discontinuous terrain, stair climbing, and mine clearance. One could argue that the engineering community has entrenched itself with mindsets developed over years of manned transport system design. With new attention being given to autonomous robotics and their use in unconditioned environments, vehicle designers must rethink the old views of ground traversal and release the assumptions inherent to traditional human-driven transport methods. This thesis rethinks one of the earlier wheeled vehicle approaches and helps develop a new class of vehicle that should be considered for autonomous applications, namely, the biplanar bicycle.

To understand the concept, consider first a pair of uniform, balanced wheels set abreast of one another and coupled by an axle pivoted at the center of each wheel. Further, assume that a mass has been added at the rim of each wheel at a point closest to the ground.

These masses will be referred to as the *reaction masses*. On level ground, such an arrangement would be stable. This arrangement is shown in Fig. 1.6.

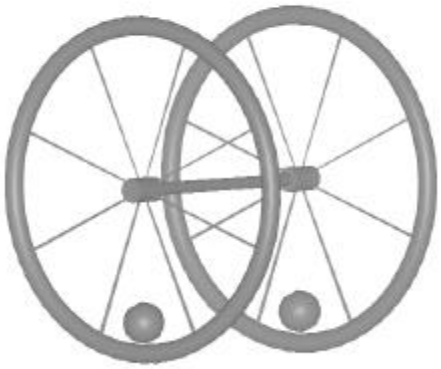

FIGURE 1.6: The Biplanar Bicycle Concept

Now assume that the masses have been moved to an unstable position, for example to the same vertical height as the axle. This arrangement is shown in Fig. 1.7. It is clear that the vehicle will begin to roll and will not come to rest until the masses are again at their minimum energy position, as in Fig. 1.6. In the absence of friction, the system will, of course, oscillate indefinitely about the stable position. Most real systems will come to rest after a few cycles of oscillation. Even so, the resulting equilibrium position will advance the vehicle by a quarter of the wheel circumference, assuming no wheel slip.

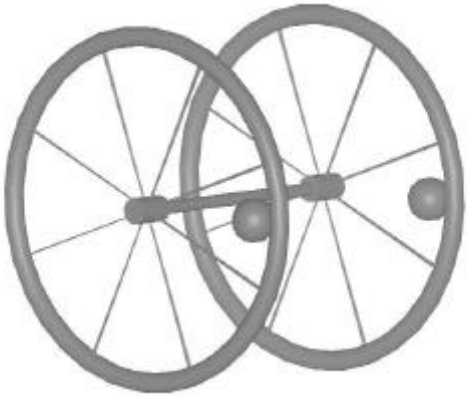

Figure1.7: Biplanar Bicycle with

Reaction Masses in the Driving Position

All that remains to create a functional biplanar bicycle is to create a means for actuating the reaction masses. This could be a motorized carriage that moves along the wheel rim on a track. An equally effective but simpler mechanical arrangement uses a motor at the center of the wheel driving an eccentric mass that moves relative to the wheel. Figure 1.8 shows an early prototype vehicle, constructed using two cordless drills and radio-controlled vehicle electronics.

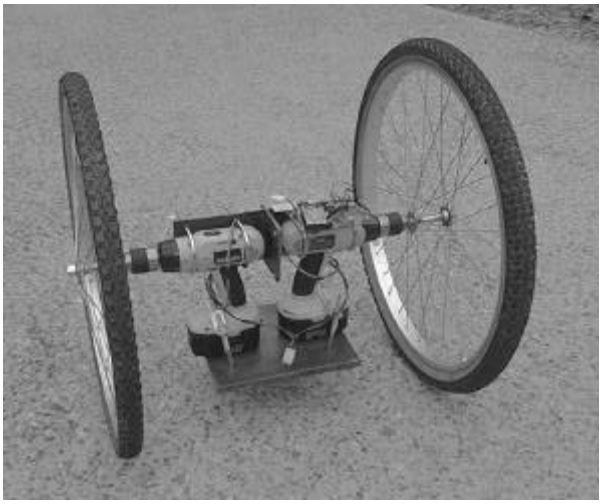

Figure1.8: Early Prototype of the Biplanar Bicycle

The use of independent drive motors and masses on each wheel allows independent control of the motion of each wheel. Alternatively, we can use a single, centrally located reaction mass and drive each wheel relative to the mass. In either case, steering is provided via differential drive. The prototype shown in Fig. 1.8 has been used to successfully demonstrate both modes of operation. The single reaction mass is mechanically simpler and has become the preferred embodiment in our work to date. Either of these configurations results in an extremely nimble vehicle that can follow any path, even those that include zero radius turns.

It seems intuitive that the biplanar bicycle would be inherently poor at traversing terrain that involved steep grades or obstacles such as stairs. However, intuition may be

misleading. In most conventional vehicles having three or more wheels, the radius of the wheels limits the size of largest single step the vehicle can ascend. This is also true of the biplanar bicycle, but, since the wheel size is large in relation to the overall vehicle, such obstacles are relatively easier to overcome. Also, since the "wheelbase" of the biplanar bicycle is zero, there is less likelihood of the vehicle becoming stranded by an obstacle wedged under its frame. The reaction mass is vulnerable to interference with the ground, especially because we would like it to be at the most extreme possible radius. Keeping the reaction mass as close as possible to the wheels, or even inside the rims of the wheels, will minimize or eliminate this concern.

The remainder of this thesis examines a simple planar model and its associated dynamics. Both static and dynamic equilibrium are considered. The issue of wheel slip is considered in chapter four, and chapter five presents vehicle performance envelops based on input waveforms. Chapter six introduces the necessary information to complete the three-dimensional dynamic simulation. The remaining chapters deal with secondary design considerations in the development of this vehicle class.

Chapter 2

Literature Review

We suggested in chapter one that ground vehicle development has traditionally been motivated by the need to move people and cargo from one location to another, always with the intent of having a human operator. Only since the inception of the microprocessor as a viable control tool has the design and use of autonomous robotics become practical. Now that we are able to remove the human operator from the vehicle, we are left with more freedom in our base vehicle design. The biplanar bicycle is awkward for transporting people, but it has great potential for use as an autonomous vehicle. As a result, this thesis appears to be the first analytical consideration of this type of vehicle platform.

Two-wheeled vehicles are not absent from the historical record. In fact, it could be argued that they appeared in some form as one of the earliest types of wheeled apparati.

Figure 2.1: The Roman Chariot

For example, figure 2.1 is an artist's representation of one of the most commonly recognized ancient two-wheeled vehicles. The roman chariot, used in warfare to speed attacks, can still be found today manifested in the sport of horse-racing. A much older and lesser-known use of the two-wheeled vehicle is manifested in an amazing example of ancient engineering effort.

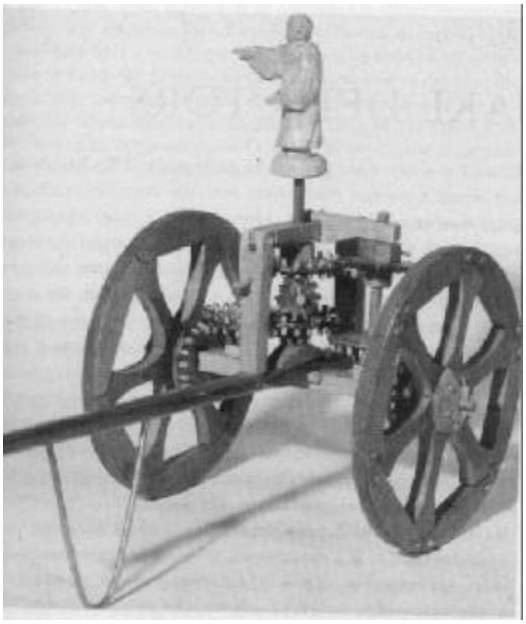

Figure 2.2: The Notorious South-Pointing Chariot

Invented in China, the notorious south-pointing chariot was intended as a navigational aid. Although its design is similar to that of the roman chariot, its operational intent is vastly different. The south-pointing chariot uses a simple differential gear train to maintain a constant pointing direction for the figure on top. This assumes the vehicle will operate under the dynamic constraint of no-slip so that the dead-reckoning navigation produced by the differential will be accurate.

Because of the ubiquitous use of two-wheeled carts, chariots, and carriages, we find it useful to further refine what we intend when describing a vehicle as a "biplanar bicycle." Consider the modified "biplanar" to the standard idea of a bicycle.

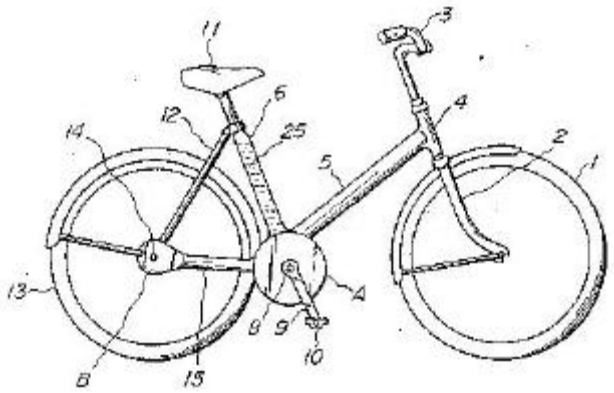

Figure 2.3: The Standard Bicycle, U.S. Patent 4684143

Figure 2.3 presents the image most commonly conjured by the term bicycle. What is important to note here is that the two wheels primarily operate within the same spatial plane, deviating only during turns. Therefore, the biplanar modifier is intended to exclude the standard bicycle and imply only vehicles containing a two-wheel, single-axle configuration. Although this restricts the definition considerably, it is not all that is needed. An inherent feature of the biplanar bicycle not implicit in the name, is the existence of only two points of ground contact. Reconsider the chariots shown in figures 2.1 and 2.2. Both of these, along with every two wheeled cart ever devised, rely on a person, pack animal, or other propulsive source to be affixed to the vehicle at a location in front of or behind the wheel axle. The result of this restriction is the creation of a third point of contact on the ground. This allows the vehicle to perform in a similar manner as

a tricycle. More importantly, it allows the vehicle to maintain a given orientation with respect to Newtonian ground. When we discuss the biplanar bicycle, we are considering only vehicles with two points of ground contact and therefore, no orientation reference. As one may imagine, this restricts our definition to a very small number of vehicles. In fact, most people have probably never seen a vehicle that falls under this strict definition. However, some do exist.

In 1998 A. Namngani was awarded a patent for a vehicle intended to move people instead of cargo. His design can, in every way, be defined as a biplanar vehicle.

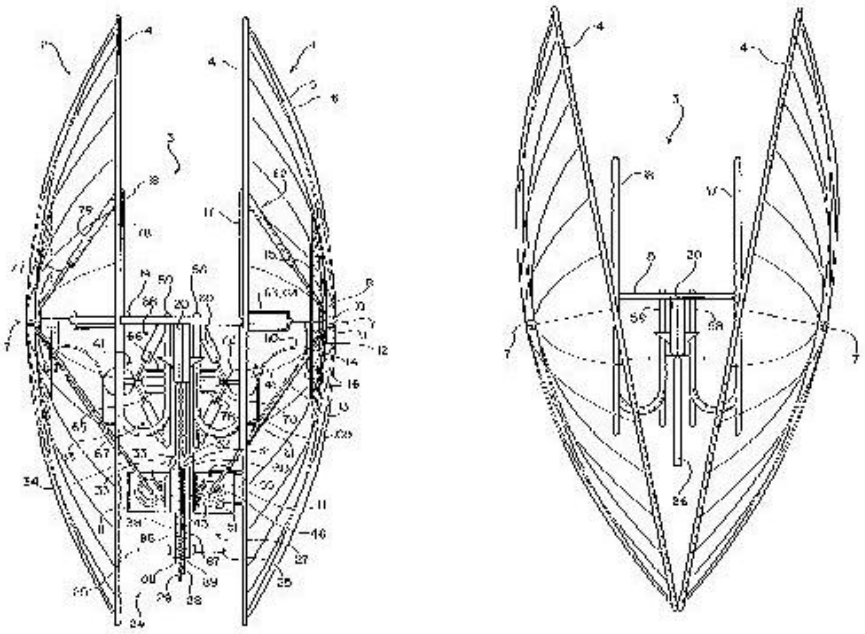

Figure 2.4: Vehicle having two axially spaced relatively movable wheels, U.S. Patent 5769441

Figure 2.4 presents Namngani's design. It is apparent from the diagram that the biplanar bicycle, when designed for human transport, can be very awkward. Although we have no confirmation on whether or not this design was physically realized, we are certain that it would have been, at best, very difficult to manufacture. There is evidence, however, that successful attempts have been made to build and operate a people-carrying biplanar bicycle.

Figure 2.5: Biplanar Bicycle built by Kriewall Enterprises, Inc.

Figure 2.5 is a fascinating example of a successful biplanar bicycle. This example is used in parades in the Romeo MI. area. Although its primary purpose is for amusement, it has all the features to make it a legitimate and operational member of our vehicle class. Beyond these two examples, very little is available to substantiate any historical use of the biplanar bicycle.

Because of the limited use of biplanar bicycles, it stands to reason that very little analytical work has ever been done to understand its dynamics. Nothing could be found in technical literature on any ground vehicles similar to the biplanar bicycle. Much work has been done on differentially driven vehicles, but our restriction of two points of ground contact makes this work unrelated. This thesis appears to present the first analytical consideration of this vehicle class.

Chapter 3

Planar Dynamic Model and Control Strategies

In chapter one we introduced the biplanar bicycle and showed that its potential performance and simplicity of manufacture make it attractive in the field of autonomous robotics. For this reason, it is important that we understand the dynamic characteristics of the vehicle. Like any new vehicle, areas of the operational envelope that remain unknown or misunderstood can eventually lead to unpredicted failure modes. We also understand from chapter two that no work has been done on the analytical kinematics and dynamics of this vehicle class. Determining a starting point for this work is therefore easy. If we know nothing, it is best to begin with a simplified but dynamically representative model.

3.1 Kinematic Model

The system can be greatly simplified by taking advantage of its inherent geometric symmetry. By only considering performance within the plane of one wheel, we remove the non-holonomic constraints normally associated with wheeled vehicles. This concept will be revisited in chapter six when the complete three-dimensional dynamics are derived. We may further reduce complexity by imposing constraint conditions of no-slip and no-bounce. One may argue these assumptions will lead to erroneous results for any

real vehicle. To assuage any fears in this regard, the fundamental concepts and validity of the no-slip and no-bounce constraints will be reconsidered in chapter four. Finally, in order to leave some generality in the solution, we assume the planar model to be rolling on an arbitrary incline of *b* degrees. The idealized planar model of the biplanar bicycle is shown in figure 3.1.

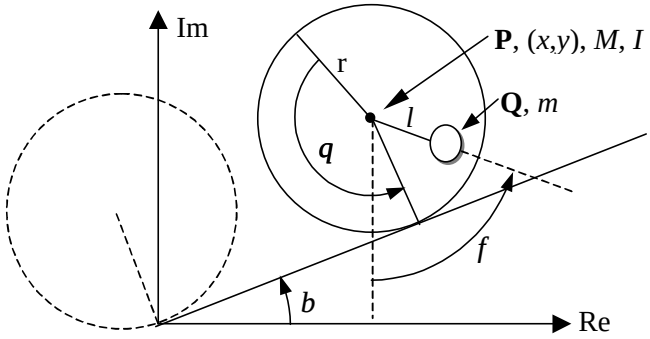

Figure 3.1: Kinematic Diagram of the Idealized Biplanar Bicycle

Any physical realization of this vehicle will, of course, have mass in all components. However, we assume here that the mass of link *l* is negligible relative to the wheel and reaction masses. This assumption can be validated through a simple thought experiment. If link *l* has substantial mass, we can combine it with the reaction mass and resize the effective link length in order to maintain the correct location for the center or mass relative to the vehicle body. By doing so, we can once again neglect the link in subsequent calculations while avoiding any loss of generality. However, we are also modeling the reaction mass as a point instead of a rigid body. The result of this assumption is a missing rotational inertia term in the kinetic energy development. The effects of this assumption, though quantifiable, are considered negligible relative to the rotational kinetics associated with the wheel. Fortunately, the assumption of zero mass for link *l* is of no consequence when analyzing the system's static and dynamic equilibria. With the kinematics defined and all assumptions made, we are ready to develop the planar dynamic model.

3.2 Planar Dynamic Model

The coordinates of the points describing the system geometry with respect to the inertial complex coordinate system are given by

$$\vec{P} = \hat{x}(\hat{t}) + j\hat{y}(\hat{t}) \tag{3.1}$$

$$\vec{Q} = \hat{x}(\hat{t}) + j\hat{y}(\hat{t}) - lje^{jf(\hat{t})} \tag{3.2}$$

where "^" indicated dimensional variables, gravity acts in the negative imaginary direction and $\vec{P}$ and $\vec{Q}$ are vectors locating the center of the wheel and the center of the reaction mass respectively. The underlying goal of creating the simple planar model is to generate a reasonable dynamic model with as few generalized coordinates as possible. Here, we impose the assumptions discussed earlier to reduce the system to two coordinates: $q(\hat{t})$ for wheel rotation and $f(\hat{t})$ reaction mass angle. The mathematical representation of the no-slip and no-bounce constraints can be described as

$$\hat{x}(\hat{t}) + j\hat{y}(\hat{t}) = r\left[q(\hat{t}) + j\right]e^{jb} \tag{3.3}$$

This completely defines $\hat{x}(\hat{t})$ and $\hat{y}(\hat{t})$ in terms of our desired generalized coordinates. This result can now be used in our original kinematic definitions for $\vec{P}$ and $\vec{Q}$ (eqs. 3.1 and 3.2). We now have enough information to determine the system kinetic and potential energy. In terms of $q(\hat{t})$ and $f(\hat{t})$ we find these quantities to be

$$T = \frac{1}{2}m\left(\dot{\vec{Q}} \cdot \dot{\vec{Q}}\right) + \frac{1}{2}M\left(\dot{\vec{P}} \cdot \dot{\vec{P}}\right) + \frac{1}{2}I\dot{q}^2 \tag{3.4}$$

$$V = mg\left(\vec{Q} \cdot j\right) + Mg\left(\vec{P} \cdot j\right) \tag{3.5}$$

To make the system more realistic, we must consider possible sources for energy dissipation. Although aerodynamic drag and rolling resistance will both be present, neither will be considered here. This is justified by the relatively slow speed (approximately 5 mi./hr.) applications for which this vehicle type was initially developed. Instead, we will only consider the damping associated with the pendulum-wheel bearing. To do so, we assume linear viscous damping and generate a Rayleigh dissipation function relating damping to the relative rotational velocity between the wheel and reaction mass.

$$R = \frac{1}{2} C\left(\dot{q} + \dot{f}\right)^2 \tag{3.6}$$

With *T*, *V*, and *R* defined we may now solve the left-hand side of the extended Lagrange equation for the dynamic response (Meirovich, 1970). This is represented as

$$\frac{d}{dt}\left(\frac{\P T}{\P \dot{q}_j}\right) - \frac{\P T}{\P q_j} + \frac{\P V}{\P q_j} + \frac{\P R}{\P \dot{q}_j} = Q_j \tag{3.7}$$

where $q = (q, f)$ and $Q = (t, t)$. At this point, the only undefined quantities for the development of the equations of motion are the generalized forces Q_j in the Lagrange equations. The only source of external energy is from the actuator used to drive the vehicle. This actuator is modeled as a simple DC servomotor and its effects transmit to both the generalized coordinates in the same way. In the development of *t* we assume a commanded input voltage resulting from a standard pulse-width-modulation control signal. Further, we neglect effects from the high-speed pole that results from armature inductance (Wolovich, 1994). The result is a mathematical description of the motor voltage as a function of motor parameters and generalized coordinates. We model the motor as

$$\hat{V}_a = i_a R_a + K_B\left(\dot{q} + \dot{f}\right) \tag{3.8}$$

which leads to

$$t = \frac{K_T}{R_a}\hat{V}_a - \frac{K_B K_T}{R_a}\left(\dot{q} + \dot{f}\right) \tag{3.9}$$

where K_B is the back electro-motive-force constant, K_T is the motor torque constant, and R_a is the armature resistance. At this point, all the information necessary to develop complete equations of motion have been derived. However, the resulting equations are rather complex and have as many as nine variables and parameters for the vehicle designer to consider while building a workable system. This problem can be greatly simplified by defining non-dimensional variables and parameters that better describe the system behavior. In doing so, we also make it a simple matter to compare the relative importance of nonlinear and damping effects in the system design.

We now introduce the following non-dimensional parameters

$$\begin{aligned} L &= \frac{l}{r} & a &= \frac{m}{M+m} \\ z &= \frac{C}{r^2 w} + \frac{K_B K_T}{R_a r^2 (M+m) w} & m &= \frac{I}{(M+m) r^2} \end{aligned} \tag{3.10}$$

and non-dimensional variables

$$U = \frac{K_T \hat{V}_a}{R_a r^2 (M+m) w^2} \quad \text{and} \quad \mathrm{t} = \hat{t} w \tag{3.11}$$

where $w = \sqrt{g/r}$. The final equations of motion may now be written in a much more tractable form and valuable information about system response and stability can be easily extracted. The equations of motion are

$$\begin{aligned} &(1+m)\ddot{q} + La\cos(b-f)\ddot{f} \\ &\quad + \left[z + La\sin(b-f)\dot{f}\right]\dot{f} + z\dot{q} + \sin(b) = U \end{aligned} \tag{3.12}$$

$$L^2 a \ddot{f} + La\cos(b - f)\ddot{q} + La\sin(f) + z(\dot{q} + \dot{f}) = U \tag{3.13}$$

Vehicle response, static and dynamic equilibrium, automatic control, and operating envelope can now be discussed in terms of non-dimensional descriptors. Furthermore, Eqs. (3.12) and (3.13) serve as useful tools in the design of this vehicle class. From this point on, reference to any of these non-dimensional characteristics will be identical in definition as those presented here. Finally, it is important to note the absence of q in Eqs. (3.12) or (3.13). This is because q is a cyclic variable and only its derivatives affect the dynamic response.

3.3 Equilibrium Conditions and Dynamic Stability

Before we can consider design or control of the biplanar bicycle class of vehicles, it would be wise to investigate the stability on a global level. To do so, we simply consider Eqs. (3.12) and (3.13). Two states of equilibrium can be easily derived. First, consider the case in which the vehicle sits stationary on an arbitrary slope of b degrees. In this limiting case, all angular velocities and accelerations reduce to be identically zero. When we enforce this condition on the equations of motion, they reduce to

$$\sin(b) = U_o \quad \text{and} \quad La\sin(f_o) = U_o \tag{3.14}$$

where, in the preceding equation, we use notation such that x_o denotes the equilibrium value of $x(t)$. It stands to reason that there exists a limiting value of slope b after which the vehicle will be incapable of holding its position. To determine this operational boundary we solve for f_o in the previous equations. The resulting solution is

$$f_o = \sin^{-1}\left[\frac{\sin b}{La}\right] \tag{3.15}$$

The inherent limitations on f occur because we cannot allow the angle to be complex. Clearly, b must be bounded above and below to ensure an inverse sine operand less than unity:

$$-\sin^{-1}(La) \le b \le \sin^{-1}(La) \tag{3.16}$$

Another interesting result from Eq. (3.15) is the implication of two equilibrium values for f_o. It will be shown that the solution in the second quadrant is always unstable. Further, the bounds associated with Eq. (3.16) correspond to stable node bifurcations at which the equilibrium solutions coalesce and disappear. This phenomenon can also be associated with the dynamic condition of whirling in which the vehicle unsuccessfully attempts to either remain stationary or climb the slope. Whirling is defined as the dynamic state in which the reaction mass makes at least one full rotation around the axle.

The second condition for equilibrium is defined by assuming the vehicle maintains a constant velocity over constant-slope terrain within the previously defined limits. This condition can also be satisfied by $\dot{f} = 0$. When this condition is enforced upon the equations of motion the resulting equation for the equilibrium velocity is

$$\dot{q}_o = \frac{U_o - \sin b}{z} \tag{3.17}$$

while the equilibrium pendulation angle continues to satisfy Eq. (3.15). However, knowing these equilibrium positions exist is not necessarily enough to understand the vehicles dynamic characteristics. It would also be helpful to know the stability of the equilibrium positions.

The stability of this dynamic equilibrium can be demonstrated using Lyapunov's linearization method (Slotine and Li, 1991). We enforce the condition for dynamic equilibrium and impose the following perturbations upon the system:

$$\dot{q} = \dot{q}_o + e\dot{q}_1(t) \tag{3.18}$$

$$f = f_o + e f_1(t) \tag{3.19}$$

where e is a small nondimensional parameter ($e << 1$). This results in the following system of equations representing the linearization of the system about the dynamic equilibrium

$$\begin{bmatrix} 1+m & La\cos(b-f_o) \\ La\cos(b-f_o) & L^2a \end{bmatrix}\begin{bmatrix} \ddot{q}_1 \\ \ddot{f}_1 \end{bmatrix} + \begin{bmatrix} z & z \\ z & z \end{bmatrix}\begin{bmatrix} \dot{q}_1 \\ \dot{f}_1 \end{bmatrix} + \begin{bmatrix} 0 & 0 \\ 0 & La\cos(f_o) \end{bmatrix}\begin{bmatrix} q_1 \\ f_1 \end{bmatrix} = 0 \tag{3.20}$$

Note that the sign of the single non-zero term in the stiffness matrix depends only on the quadrant of f_o. Thus, our assertion about the stability of the static equilibrium points given by Eq. (3.15) has been demonstrated. Taking the Laplace transform of the system in Eq. (3.20) yields an eigenvalue problem whose solution is given by the roots of the characteristic polynomial:

$$s\left\{[(1+m)s+z]\left(L^2a\,s^2 + z\,s + La\cos f_O\right) - s[La\cos(b-f_O)s+z]^2\right\} = 0 \tag{3.21}$$

We note that the single pole at zero corresponds to the cyclic coordinate q (in control terms, we have developed a non-minimum state realization). The stability of the remaining subset of poles may be verified using the Routh-Hurwitz technique. The analysis demonstrates that, under the conditions of Eq. (3.16), the constant-forward-speed equilibrium is stable for all physical values of the design parameters.

After performing a Routh-Hurwitz stability analysis of this system, one might conclude that this system is stable. This is to say, any command voltage will eventually result in a steady state, controlled forward velocity. However, we will see that this is not the case. This leads to the conclusion that simple linear control of this system may not yield a sufficiently robust design. It is therefore expected that a more complex, nonlinear control algorithm will be needed if we expect to control this class of vehicle throughout its operational envelope of terrain, velocity, and acceleration. These nonlinearities are easily demonstrated with the numerical solutions to the original, non-dimensionalized equations of motion.

3.4 Numerical Simulations and Demonstration of Nonlinear Effects

Numerical integration of the governing equations provides an environment for simulation of the system response. Such a simulation environment is useful for developing understanding and intuition about the system, and provides a tool that can be applied to feedback control-law development. Macro-scale influences of the nonlinearities (i.e., far from equilibrium conditions) are exhibited in the system's open-loop (i.e., uncontrolled response). For example, consider upward traversal of a five-degree grade. As might be expected, higher step-input voltages result in larger pendulation angles f during the transient (Fig. 3.2). While the steady-state velocity depends only on the voltage, and the steady-state pendulation angle depends only on the slope, transient overshoot pendulations are expected because the reaction mass is the source of acceleration. Thus, increasing the voltage step (that is, the set-point of steady-state velocity) increases the overshoot. Of course, such an overshoot increase provides improved response only until the pendulation angle reaches ninety degrees. Any further increase in the applied voltage will result in a demand for more leveraging resistance than the rotating mass can provide through gravitational potential. The result is whirling. Once f exceeds the unstable equilibrium and whirling begins, it is unlikely that direct application of an open-loop control strategy will result in the vehicle reaching the desired forward-speed equilibrium. During whirling, a significant fraction of the motor's energy becomes stored as kinetic energy of the pendulum mass, leaving the two-wheeled vehicle at the mercy of the slope. The result is a dynamic equilibrium with a net down-slope velocity. Figure 3.3 illustrates

the new, stable, dynamic equilibrium. Even at steady state the reaction mass continues to whirl (i.e., exhibits a limit cycle behavior), resulting in a similar limit cycle in wheel velocity, but with a negative DC offset.

We stress that the new equilibrium behavior exhibited by the system does not represent a destabilizing bifurcation of the steady-forward-speed equilibrium. According to Routh-Hurwitz analysis, the target equilibrium retains its stability: clearly an alternative solution exists. The initial conditions and DC voltage amplitude dictate the final equilibrium response of the vehicle. As Figs. 3.2 and 3.3 indicate, the nonlinear nature of the problem can result in unexpected responses. The equilibrium's basin of attraction boundary generates a sharp contrast in the behavior of the nonlinear system. Figures 3.2 and 3.3 have the same initial conditions and differ by only one ten thousandth in nondimensional input voltage.

Although the constant-forward-speed equilibrium has been shown to be universally stable, numerical simulations argue against simple open-loop command. Feedback control may provide the desired consistency of performance.

3.5 Non-Traditional Rate-Feedback Control

The governing dynamic equations of the two-wheeled vehicle have been shown to be nonlinear even under the simplifying assumptions of planar operation and slowly varying terrain. Numerical simulations have demonstrated that such nonlinearities cannot be neglected. The equilibrium deflection of the reaction mass depends on the slope. This highly variable parameter proscribes a single linearized approximation to the vehicle dynamics. This motivates the application of a simple heuristic control law, developed with the aid of numerical simulation, rather than the application of traditional linear control theory.

The control law should provide for effective reference tracking. The nature of the stable steady-forward-speed equilibrium suggests a nonlinear feedback algorithm for

developing zero steady-state error. Recall Eq. (3.17), which dictates the required nondimensional voltage for a particular velocity:

$$U_o = z\dot{q}_o + \sin b \tag{3.22}$$

It seems that it may be effective to compose a command voltage of

$$U(t) = z\dot{q}_{ref} + \sin b + \tilde{U}(t) \tag{3.23}$$

where $\tilde{U}(t)$ is governed by a feedback control law. It is intended to have a regulating effect, and it should approach zero as the system approaches equilibrium. Equation (3.23) has a fundamental flaw, however. It is unlikely that b will be known *a priori* and real-time measurement of b is potentially difficult. Equation (3.14) suggests that the control law can instead be written in terms of the equilibrium value of f. Because f_o is also unknown, the necessary term in the control signal can be approximated by a nonlinear state-feedback term:

$$U(t) = z\dot{q}_{ref} + aL\sin f(t) + \tilde{U}(t) \tag{3.24}$$

The closed-loop system exhibits zero steady-state error (assuming its steady state is the target equilibrium). Tracking, while meeting a design requirement, does not provide the robust performance we seek. The enhancement $\tilde{U}(t)$ to the control signal is composed of linear feedback terms that seek to improve the transient response of the system (i.e., provide regulation). Because our system exhibits zero steady-state error, the primary objective of the regulation is to prevent the whirling of the reaction mass. Rate feedback is traditionally used to prevent excessive overshoot through an increase in the effective linear viscous damping of the system. Rate feedback can be applied through both the pendulation and wheel-fixed coordinates. System overshoot is controlled by the positive derivative feedback gain K_d associated with the pendulum angle f. This gain is increased until the resulting reduction in overshoot no longer justifies the subsequent increase in

system response time; recall that some overshoot is intrinsically necessary in the response to produce accelerations. Thus while a small amount of rate feedback dramatically reduces overshoot, a large amount has little additional effect.

Experimentation with a proportional feedback gain K_p applied to the rate of the cyclic variable q shows that this variable does not significantly influence the overshoot. Rather, it has a moderate effect on the speed of response. Some portion of the increased system response time can be recaptured through *negative* rate feedback on this coordinate. While the speed of response is not as important as the tracking and overshoot criteria, it is sufficiently important to justify the resulting robustness tradeoff. Here, the robustness in question is associated with model uncertainty; a sufficiently large error in the modeling of plant parameters could destabilize the target equilibrium in a Lyapunov sense. The control law presented here has been developed numerically for generalized non-dimensional geometry. To aid its use, the dimensioned control algorithm is presented here as

$$\begin{aligned}\hat{u} = \frac{\dot{q}_{ref}}{r^2}\left[C + \frac{K_B K_T}{R_a\left(M+m\right)}\right] + \frac{ml}{(M+m)r}\sin f \\ + \left[0.8\left(\dot{q} - \dot{q}_{ref}\right) - 10\dot{f}\right]\sqrt{\frac{g}{r}}\end{aligned} \tag{3.25}$$

The implementation of this control law demonstrates its ability to moderate pendulum motion and smooth the vehicle velocity profile. Figure 3.4 shows both open- and closed-loop dynamic response of the pendulum angle f and wheel rotation angle q as function of non-dimensional time. All simulations were performed using the following system geometry:

$$\begin{aligned} L = 0.8 \qquad a = 0.9 \qquad z = 0.2 \\ m = 0.066 \qquad b = 0.0873 \qquad K = 2 \end{aligned} \tag{3.26}$$

This completes the analytical development of the planar kinematic and dynamic models. A solid understanding of the concepts presented here is enough to allow the design engineer to build a vehicle. The problems resulting from system nonlinearity and non-holonomic constraints out of the plane will most likely be of little consequence during most vehicle applications. However, these issues are explained in detail in subsequent chapters in case they prove important during implementation.

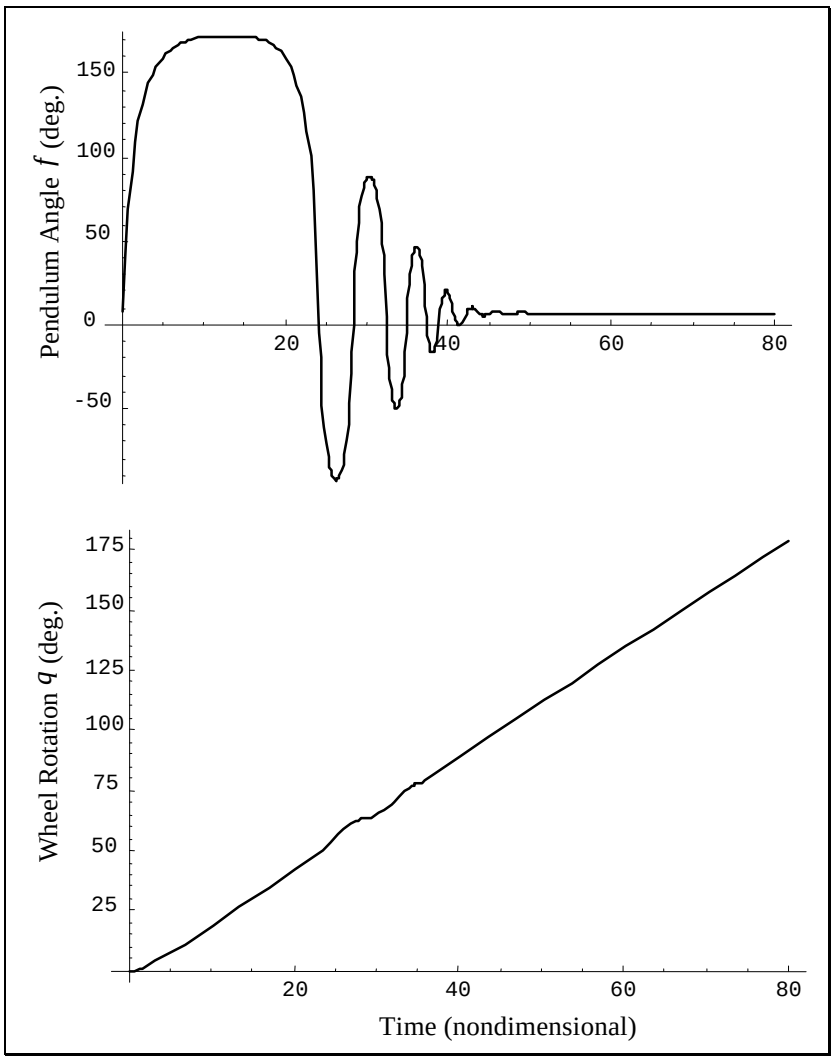

Figure 3.2: Open-Loop Step Response, *U*=5.0344

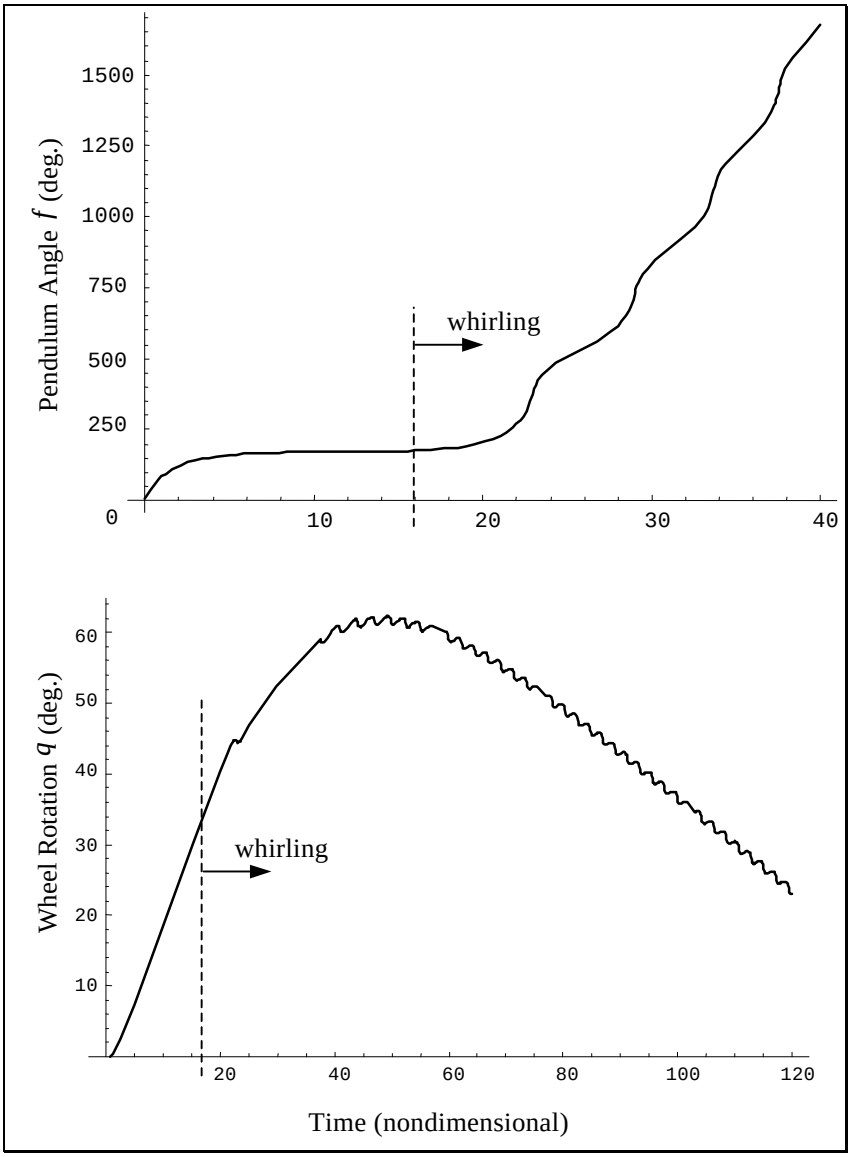

Figure 3.3: Open-Loop Step Response, *U*=5.0345

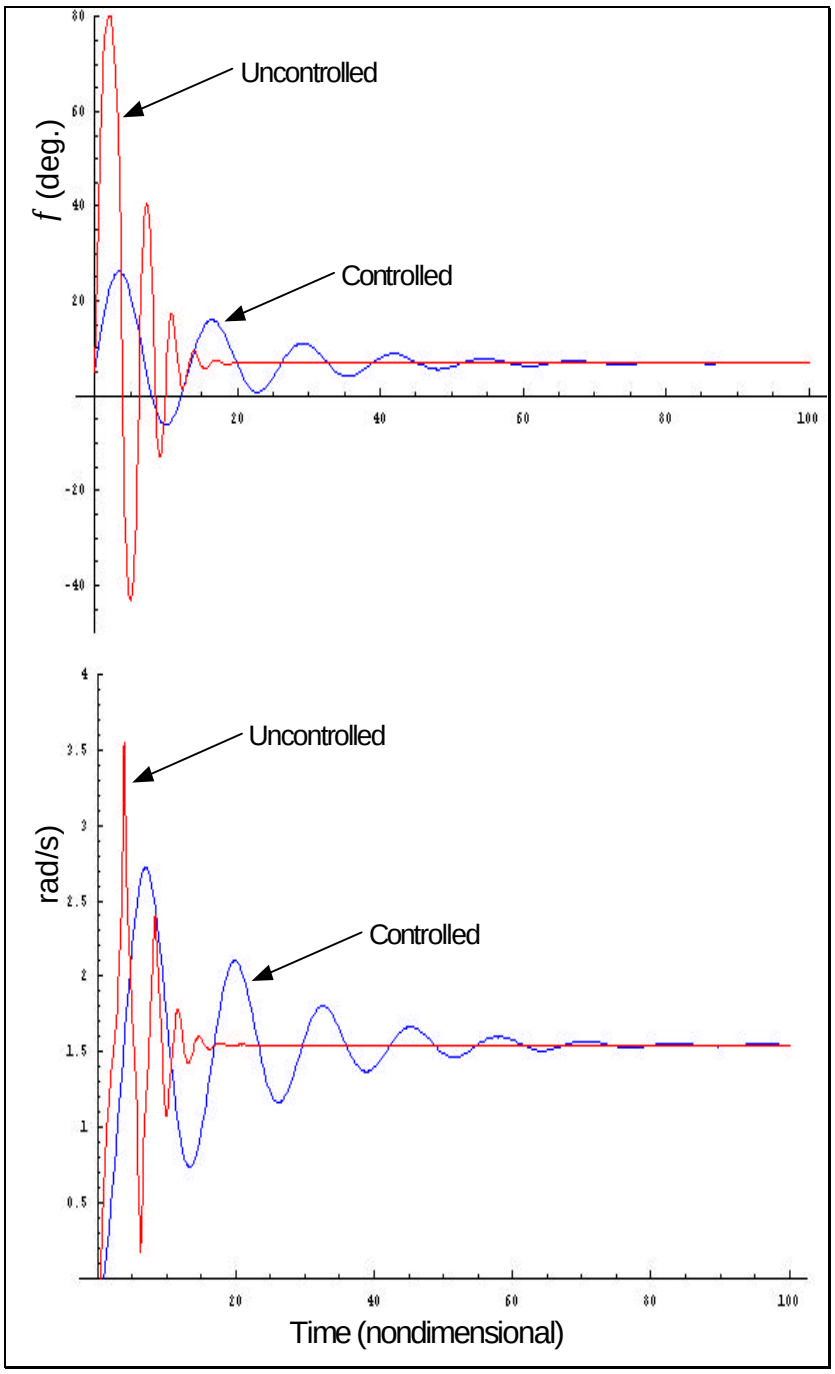

Figure 3.4: Uncontrolled and Controlled (K_p = -0.8, K_d = 10) Responses.

Chapter 4

Investigation of Planar Vehicle Slip Conditions

In the previous chapter we developed and analyzed the complete planar dynamic system of the simplified Biplanar Bicycle model. During that development we imposed certain kinematic constraints and assumptions to make the underlying mathematics more tractable. In doing so, we generated useful information regarding dynamic response and behavioral bifurcation. Further, we were able to distinguish certain operational regimes in which the vehicle can and cannot operate. These performance envelopes will be discussed in greater detail in the next chapter. Here, we are concerned with rethinking the underlying assumptions in the primary planar model.

4.1 Kinematic Model

The most important kinematic constraints imposed in chapter three are those of pure rolling and no bouncing. From a kinematic standpoint, we effectively reduced the mobility of the entire system by a single degree of freedom, thus simplifying the dynamic analysis. Pure rolling is defined as the kinematic relationship of a rigid wheel rolling across terrain such that the relative velocity between the wheel and the ground along the common tangent at the contact point remains identically zero. Figure 4.1 diagrammatically demonstrates this concept.

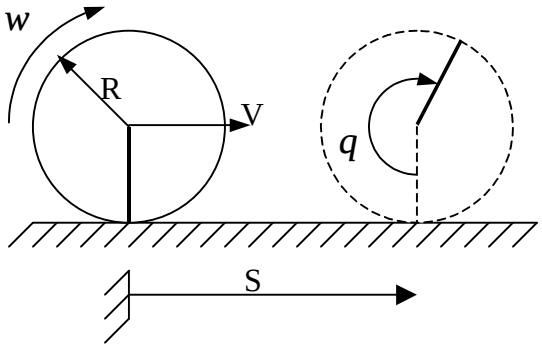

Figure 4.1: Kinematic Diagram of Pure Rolling

Note that the constraint, in its pure mathematical form, does not necessitate the wheel and ground to be in direct contact.; it simply provides a relationship between angular and linear (along the common tangent) displacement. If the system acts under the no-slip constraint, the following kinematic relationship governs position in the direction of the common tangent.

$$S = Rq \qquad V = Rw \tag{4.1}$$

The no bounce constraint, like that of no-slip, removes a degree of freedom associated with translation. In this case, the relative velocity of the wheel center and the plane is identically zero in the direction along the common normal. The constraint associated with enforcing no bounce is simply that of maintaining a constant distance (radius of the wheel) between the wheel center and the contact plane. In other words, the wheel must neither lose contact with nor impinge upon the plane.

Frictional forces are related directly to the no-slip constraint. It is the wheel-plane frictional interaction that prevents slip in any real system. Likewise, the frictional force capable of being produced is directly related to the normal force involved in maintaining the no-bounce condition. Therefore, if we are concerned with whether the biplanar bicycle will exhibit slip in any given operational scenario, both the frictional and normal

forces must be accounted for during the dynamic analysis. However, the Lagrangian approach used in chapter three is designed to ignore internal constraint forces such as friction and contact forces. We must modify the dynamics in order to see how these forces are being manifested during operation. The explanation of how this is accomplished is discussed in the next section. First, we revisit the kinematic definitions of the planar model as developed in chapter three. The inertial frame in this case is coincident with the inclined plane. The kinematic diagram of this system is shown in figure 4.2.

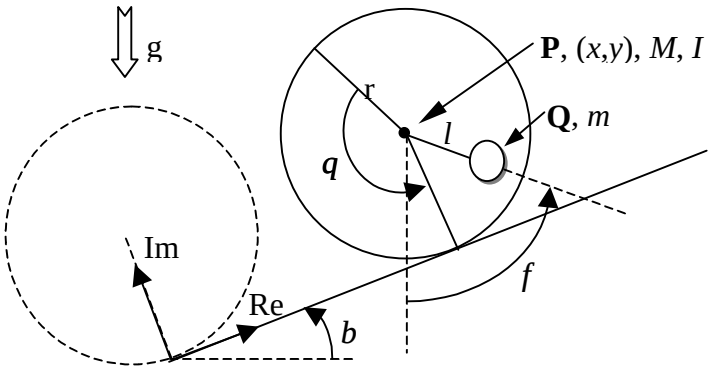

Figure 4.2: Kinematic Diagram of the Idealized Biplanar Bicycle

The coordinates describing the system geometry with respect to the now rotated inertial complex coordinate system are presented here as

$$\vec{P} = \hat{x}(\hat{t}) + j\hat{y}(\hat{t}) \tag{4.2}$$

$$\vec{Q} = \hat{x}(\hat{t}) + j\hat{y}(\hat{t}) - \hat{l}je^{j(f(\hat{t})-b)} \tag{4.3}$$

where the real axis is now parallel to plane of slope b, and $\vec{P}$ and $\vec{Q}$ are vectors locating the center of the wheel and the reaction mass respectively. Unlike the model in chapter three, we cannot use no-slip and no-bounce to simplify Eqs. (4.2) and (4.3). Instead, $\hat{x}(\hat{t})$ and $\hat{y}(\hat{t})$ must remain as two additional generalized coordinates. $\hat{x}(\hat{t})$ is associated with

the wheel position tangent to the slope face (**Re**) and $\hat{y}(\hat{t})$ defines the wheel's position along the common normal (**Im**). Instead of constraining these coordinates as was done in chapter three, they are left free so we can later calculate the force required ensure that they remain in their previously constrained positions.

4.2 Slip Investigation Dynamic Model

The dynamic system now contains four generalized coordinates: two from the original model and two new ones associated with the relaxed slip and bounce constraints. However, the addition of these variables is necessary but not sufficient to yield the solution of the revised system. We must also add new forces to account for our added degrees of freedom. We accomplish this by developing Lagrange Multipliers associated with each new degree of freedom. These will be described in more detail later as we do not require them to develop the system energy equations.

Unlike the original planar no-slip no-bounce model, we have defined the inertial reference in a direction such that gravitational acceleration does not coincide with the imaginary axis. If the plane has slope b, the direction of the increasing potential field is

$$\hat{G} = je^{-jb} \tag{4.4}$$

We note that $\vec{P}$ and $\vec{Q}$ may now be expressed in terms of the fundamental generalized coordinates $q(t)$, $f(t)$, $x(t)$, and $y(t)$. The resulting kinetic and potential energy is given by

$$T = \frac{1}{2} m\left(\dot{\vec{Q}} \cdot \dot{\vec{Q}}\right) + \frac{1}{2} M\left(\dot{\vec{P}} \cdot \dot{\vec{P}}\right) + \frac{1}{2} I\dot{q}^2 \tag{4.5}$$

$$V = mg\left(\vec{Q} \cdot \hat{G}\right) + Mg\left(\vec{P} \cdot \hat{G}\right) \tag{4.6}$$

Additionally, we can maintain the same Rayleigh dissipation function used in chapter 3 to model a linear viscous damping effect in the pendulum-wheel bearing.

$$R = \frac{1}{2} C\left(\dot{q} + \dot{f}\right)^2 \tag{4.7}$$

With these energy definitions complete, we must turn attention to the new kinematic constraints associated with the relaxed slip and bounce conditions. The most efficient method to check slip without deviating far from the original planar model is to employ Lagrange multipliers to track internal constraint forces. The constraints associated with no-slip and no-bounce are

$$\hat{r}q(\hat{t}) - \hat{x}(\hat{t}) = 0 = C_f \tag{4.8}$$

$$\hat{y}\left(\hat{t}\right) - r = 0 = C_n \tag{4.9}$$

respectively. Imposing a Lagrange multiplier on each of the constraint equations and differentiating with respect to each of the generalized coordinates produces the generalized forces associated with friction along the plane and contact along the common normal. The general form of this derivation is

$$Q_j = \sum_i l_i \frac{\partial C_i}{\partial q_j} = l_f \frac{\partial C_f}{\partial q_j} + l_n \frac{\partial C_n}{\partial q_j} \tag{4.10}$$

This calculation results in generalized forces that will supplement the right hand side of the extended Lagrange equation (Meirovich, 1970). These forces can be shown to be

$$Q_q = r l_f \qquad Q_f = 0 \qquad Q_x = -l_f \qquad Q_y = l_n \tag{4.11}$$

From this point the governing dynamic equations of motion can be derived using the extended Lagrange equation

$$\frac{d}{dt}\left(\frac{\partial T}{\partial \dot{q}_j}\right)-\frac{\partial T}{\partial q_j}+\frac{\partial V}{\partial q_j}+\frac{\partial R}{\partial q_j}=Q_j \tag{4.12}$$

where $q=(q,f,x,y)$ and $Q_j = f(t,t,l_f,l_n)$.

The drive torque t is again modeled as a simple DC servomotor including consideration of both applied voltage and back electromagnetic force. If the armature inductance is ignored, the applied armature voltage is

$$\hat{V}_a = i_a R_a + K_B\left(\dot{q}+\dot{f}\right) \tag{4.13}$$

This leads directly to an expression for the motor torque t.

$$t = \frac{K_T}{R_a}\hat{V}_a - \frac{K_B K_T}{R_a}\left(\dot{q}+\dot{f}\right) \tag{4.14}$$

Where K_B is the back EMF constant, K_T is the motor torque constant, and R_a is the armature resistance. Equations (4.8), (4.9), (4.11), (4.12), and (4.14) describe a system whose input is the applied armature voltage and whose output is the dynamic response of the four generalized coordinates *q(t), f(t), x(t),* and *y(t).* Further, both the normal and frictional contact forces are found by solving for the two multipliers l_n and l_f. These may be compared with respect to a predetermined static friction coefficient to determine whether or not the vehicle slips.

4.3 Numerical Simulations

Now that a complete dynamic model has been built, it is important to verify whether the issue of vehicle slip even enters into a normal operational envelope. We have seen in chapter three that the whirling phenomenon is a limiting factor on input voltage.

Therefore, we must only determine if slip is likely at voltages less than that of whirling. If so, we can conclude that slip has the potential to tighten the operational envelope. A simple thought experiment can show the potential for slip problems. Imagine the vehicle at rest on a level plane. If the coefficient of static friction between the wheel and ground is identically zero, the wheel will slip for infinitesimally small input voltages. In fact, any commanded input will yield countering motion in both the reaction mass and the wheel. However, the existence of slip in the limiting case does not predicate a problem in normal operational environments. Therefore, numerical simulations need to be run if we expect to prove or disprove slip as a significant effect.

To do so, we return to the simulation model of chapter three. Using identical geometry and dynamic parameters we can calculate how much friction is required to prevent slip and how much friction is available from the instantaneous normal force. The only additional parameter required is the coefficient of static friction. To generate a test case that is likely to slip, we consider one of the suggested operational applications of the biplanar bicycle: the autonomous railway inspection vehicle. In this case we would expect the possibility of having steel wheels on a steel surface with grease at the interface. The approximate coefficient of static friction in this extreme case is 0.005 [Avallone, 1987].

Finally, we must define a reasonable metric with which to judge the vehicle performance. In this case, we normalize the friction required to prevent wheel slip with the product of the frictional coefficient and normal contact force. The resulting value can be considered an instantaneous percentage of total available frictional effort. If the metric is below 100% at any given time, the system exhibits the no-slip constraint presented earlier. If the normalized friction is greater than 100%, there is not enough contact force to induce the friction needed to prevent wheel slip and the no-slip constraint is violated. At the same time, we must track the normal force acting at the contact point to ensure it never drops below zero. If it does, the system has violated the no-bounce condition and is "jumping" off the contact surface.

Figure 4.1 shows the simulation results from identical conditions found in the chapter-three model.

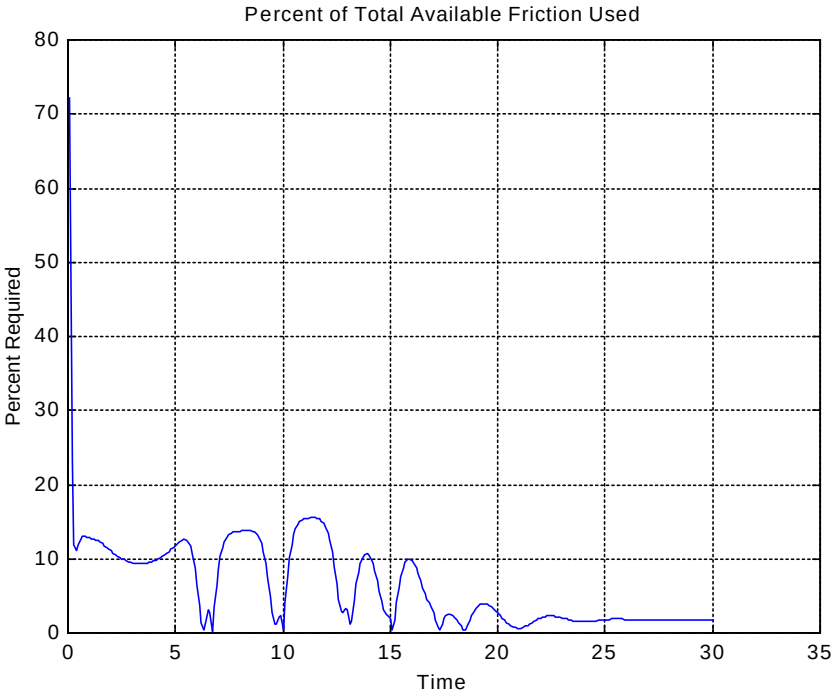

Figure 4.1: Required friction normalized to total available friction

As might be expected, the required normalized friction is highest as soon as the step input is applied. Eventually, the required friction reaches a steady-state value as the reaction mass reaches its steady-state position. The locations in which the normalized friction seems to hit singularities near zero result from the reaction mass swinging through the common normal where the contact force reaches its maximum. The spikes in these regions are simply results of numerical resolution during the simulation. Figure 4.2 presents the constituent parts of figure 4.1 in an attempt to provide greater insight to how the slip metric is produced.

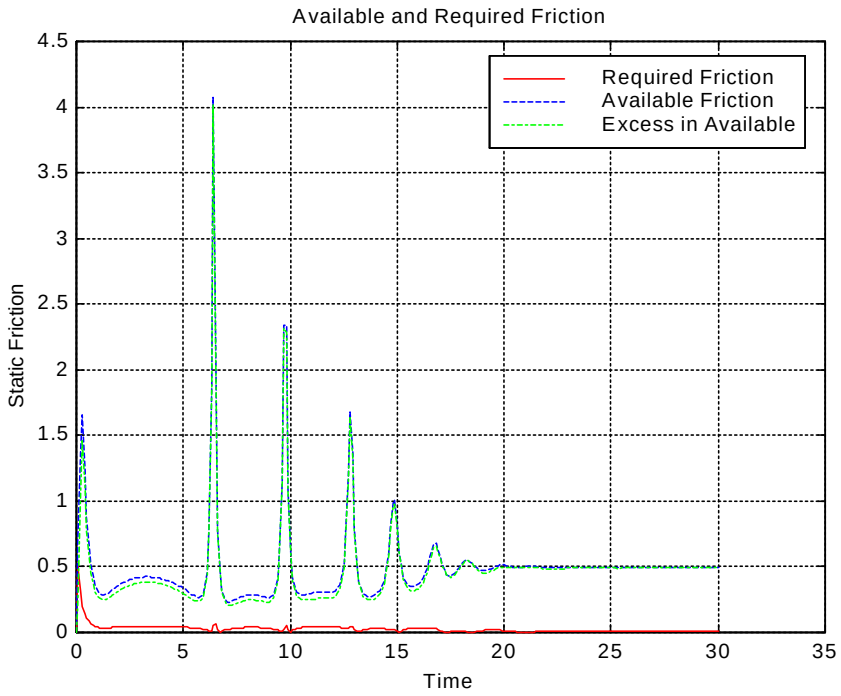

Figure 4.2: Constituent elements of the slip condition metric

As seen here, the forces required to maintain the no slip constraint are relatively low when compared to the dynamic forces being imparted during operation. Many other simulations similar to those presented here have been run and examined to ensure the validity of the model results. From these, the conclusion is made that vehicle slip does not enter into any reasonable biplanar bicycle application. Instead, the whirling effect remains the definitive boundary to the performance envelope. To verify this conclusion, the simulation was run using a high-voltage, short-duration pulse input. Although the input would be large enough to induce whirl, it is cut off before the pendulum can reach the bifurcation point. As expected, the large initial torque causes the vehicle to slip. Also as expected, as the input voltage is dropped and duration increased until we are again using a step input, the whirling condition, not slip, stands out as the limiting dynamic effect. The complete performance envelope will be discussed in more detail in chapter five.

Chapter 5

Performance Envelope of the Planar Biplanar Bicycle

In chapter three we saw that non-linear effects in the dynamic behavior of the biplanar bicycle are significant. In particular, a bifurcation point exists at which the stable and unstable dynamic equilibrium points coalesce and disappear. It is this phenomenon that makes a robust control strategy necessary if we expect to maintain control of a real vehicle. In fact, it was the avoidance of the bifurcation point that motivated the control strategy presented in chapter three. This chapter considers the whirling problem from a slightly different perspective. Because we have no analytical descriptor for the bifurcation point, the control law development of chapter three did not contain a feedback term based on the proximity of the operational point to that of the bifurcation. However, it stands to reason that the control effort can be limited if we know how close the current operational condition is to matching those of the dynamic node. Here, we present a numerical analysis of the vehicle operational envelope as a function of slope b. In addition to understanding the general shape of the envelope, an attempt is made to understand the effects of specific input waveforms on vehicle performance.

5.1 Envelope Generation

The numerical solution of the performance envelope is straightforward. The techniques used to generate solutions are universal to all vehicle configurations. Still, it is imperative that the designer understands that the results presented here are based on a single vehicle geometry, and they will change if the non-dimensional descriptors are modified. Based on several configuration simulations, we have validated the universality of envelope shape and relative sizes, regardless of changes in vehicle parameters.

To generate a single performance envelope, the equations of motion developed in chapter three are numerically solved for a given slope and input until the bifurcation point is located. The slope is increased and another search is initiated until the bifurcation is located. This process is repeated until the slope and corresponding input voltage equal the limiting values for static equilibrium as presented in chapter three. As stated before, this process is used for a variety of waveforms. All waveforms (with the exception of the step) reach their respective final voltage value in the same period of time. This permits a better qualitative analysis of their respective performances. Input types investigated are shown in figure 5.1. The letter ***T*** designates the time period over which the input waveform takes to reach steady-state.

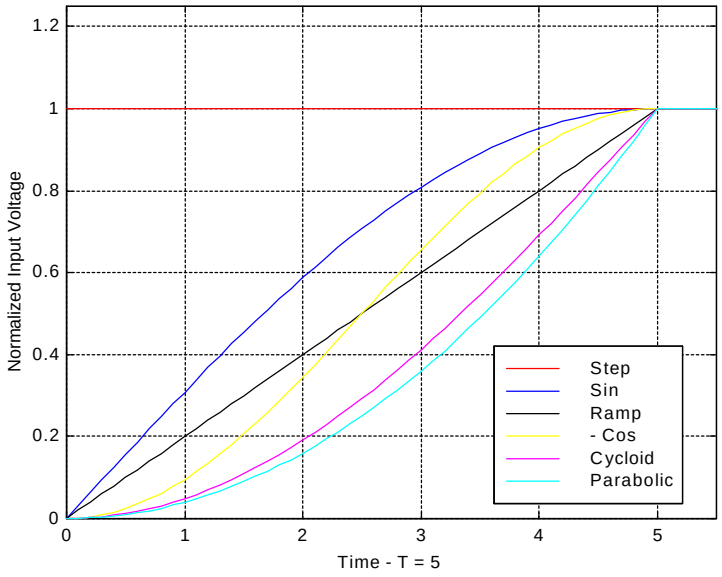

Figure 5.1: Waveforms for Vehicle Input

In this study, we are primarily concerned with how we reach the final voltage and consider the discontinuity in voltage after reaching the desired value to be of little concern. Consequences that result from not smoothing the waveforms will be left as a field for future research.

Finally, we must also consider the initial conditions from which we begin applying input. Since we wish to investigate performance for a range of slopes b, it makes sense to normalize the input to a standard reference voltage. If we consider a commanded motion from the static equilibrium point the appropriate reference voltage would be that needed to remain stationary on an arbitrary slope as discussed in chapter three.

5.2 Performance Envelope

Figure 5.2 illustrates the results of the performance envelope calculations described above for $\boldsymbol{T} = 5$. As $\boldsymbol{T}$ is increased all these input curves tend to coalesce.

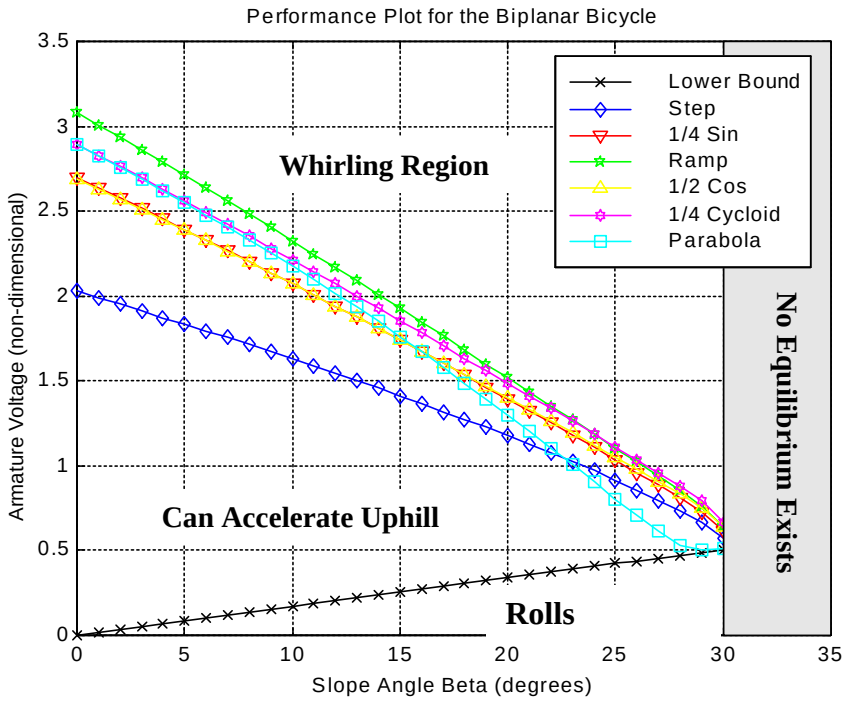

Figure 5.2: Performance envelopes for various input waveforms.

There are several interesting conclusions that may be drawn from the performance envelope study. Perhaps the most important and influential observation from the perspective of control strategy design is the relative difference in maximum input voltage between the various waveform types at any given terrain slope b. We saw in chapter three that every input voltage within the operational envelope results in finite forward velocity equilibrium. Therefore, the greater the steady state input voltage for a given b, the faster the vehicle will move at dynamic equilibrium. Here, we see the ramp input allows the highest voltage increase over a finite time span. This is a particularly attractive result when considering vehicle control since its implementation in hardware and software requires minimal effort.

The use of a ramp function as input makes the control signal generation simple to implement. We may further justify the use of ramp inputs by considering what happens if the controller is discrete (as may be expected in a real vehicle). We have not only demonstrated that the ramp is the best for an arbitrary change in voltage, but we have also shown that the step input falls short of every other input type. If we assume the vehicle controller is digital, any input waveform will consist of many small step inputs. Though undesirable, this is for the most part an unavoidable consequence caused by zero-order-hold digital to analog conversion. To avoid whirling, we would like to minimize the step change between any two time-intervals. In comparing two arbitrary waveforms, the minimum step change is associated with the waveform with the smallest instantaneous first derivative. Therefore, if we optimize any input function between two given points based on minimizing the peak of the first derivative, the resulting curve is a line (or ramp) connecting the endpoints. This heuristic argument is the simplest way to understand why the ramp input allows the largest change in input voltage in the shortest time.

Because we have already proven the relationship between command voltage and steady-state wheel velocity, it is a simple step in logic to assert that the ramp input will ultimately result in a higher maximum speed on any given slope. It must be remembered

that this result is, in the most general case, dependent on the input time period ***T***. If interest lies in fast response times, this result is of great significance. However, we still have not gained any insight concerning the development of a control feedback term based on control proximity to the bifurcation point. Unfortunately, the Lyapunov exponent and Fiegenbaum's number are the only tools available to deal with the locations of bifurcation points. Although accurate, neither lends itself to the quick prediction of a system's first bifurcation. Further, if the slope changes, the nodal points would change as well. Therefore, the incorporation of a control term based on the proximity of operation to bifurcation is not a viable option. Further, if the performance envelope for a specific vehicle is developed numerically, it would be a much easier and probably more robust measure to simply regress the data, introduce a factor of safety and hard-wire the nodal locations into a slope-adaptive control algorithm.

Biplanar bicycle performance envelopes, regardless of geometry or non-dimensional parameters, take on the form presented here. The ramp input prevails in all designs as the input with the largest operational envelope. However, it must be remembered that each specific design configuration will result in a numerically different envelope and should be simulated prior to the development an adaptive linear controller.

Chapter 6

3-D Dynamics on an Arbitrarily Inclined Plane

By this point we have investigated and learned quite a bit about the dynamics of the biplanar bicycle. We have demonstrated complex non-linear behavior including behavioral bifurcation, Lyapunov stability characteristics, and some heuristic control techniques to avoid the unattractive operational regime of whirling. However, the study thus far has been confined to the plane and the effects of two wheels being driven off one reaction mass have not been considered. There are two primary reasons why the full 3-D model has not been stressed as highly as the planar system. First, the relative importance of parameters such as viscous damping and non-linear terms are easily discerned in the planar model. The mathematics in the three-dimensional model, as will soon be demonstrated, are much more complex and subsequently more difficult to dissect into informative results. Second, the present application of the vehicle class has been restricted to low-speed autonomous ground vehicles. The planar model is sufficient to explain design criteria necessary to physically construct such a vehicle. The only missing information involves the control of navigation. However, the control on biplanar bicycles turning at low speed does not deviate substantially from that of more common differentially driven three and four-wheeled vehicles.

During the 3-D vehicle's linear traversal of an inclined plane, its governing dynamics are the same as those developed for the planar model. Only during turns does it perform differently. Without any design constraints on navigation we are left to an arbitrary inspection of the 3-D dynamics. It is for this reason that we only derive the information necessary to calculate the equations of motion and provide neither solutions nor simulations to the resulting system. That work will be left to future researchers who need specific results for specific applications.

6.1 Kinematic Model

Figure 6.1 presents the idealized kinematic diagram of the three-dimensional biplanar bicycle. The side view is identical to the planar model of chapter three with the exception of an additional wheel and associated angular coordinate.

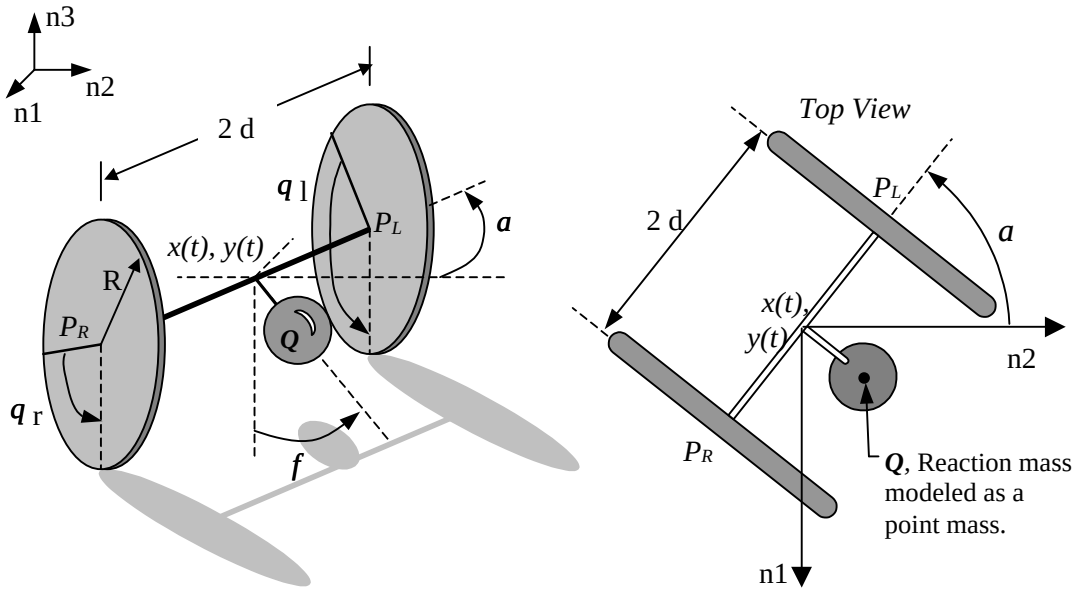

Figure 6.1: Kinematic Diagram of the 3-D Bicycle

It becomes immediately evident that the complexity of the system definitions has increased substantially. Like the planar model, we first define the positions of all body masses in terms of the Newtonian fixed reference frame (denoted by $\hat{n}$). However, because the complex number notation used previously can only be implemented with a

planar system, we are forced to revert to Cartesian definitions. The reaction mass is still modeled as a point mass and is located by

$$\vec{Q} = [x + l\sin f\cos a]\hat{n}_1 + [y + l\sin f\sin a]\hat{n}_2 + [R - l\cos f]\hat{n}_3 \tag{6.1}$$

where (x,y) denote the projected position of the axle center on the x-y plane. The only other inertial elements present within this system are the wheels. We therefore define their respective centers of mass as

$$\begin{aligned}\vec{P}_R &= [x + d\sin a]\hat{n}_1 + [y - d\cos a]\hat{n}_2 + [R]\hat{n}_3 \\ \vec{P}_L &= [x - d\sin a]\hat{n}_1 + [y + d\cos a]\hat{n}_2 + [R]\hat{n}_3\end{aligned} \tag{6.2}$$

When compared to the relatively simple position vectors derived in chapter three, Eqs. (6.1) and (6.2) prove substantially more complicated.

6.2 System Energies

The process for developing the kinetic and potential energies remains the same as the planar model. We must simply account for more inertial elements and time-dependent system coordinates. The kinetic energy can be shown to be

$$T = \frac{1}{2}\left[m\left(\frac{D\vec{Q}}{Dt}\cdot\frac{D\vec{Q}}{Dt}\right) + M\left(\frac{D\vec{P}_R}{Dt}\cdot\frac{D\vec{P}_R}{Dt} + \frac{D\vec{P}_L}{Dt}\cdot\frac{D\vec{P}_L}{Dt}\right) + I_R\dot{q}_R^2 + I_L\dot{q}_L^2\right] \tag{6.3}$$

where: m = Mass of Reaction Mass
M = Mass of a Single Wheel
I_R = Right Wheel Inertia
I_L = Left Wheel Inertia (nominally same as right)

Taking the inner product of the mass position vectors with the local potential field generates the potential energy term. Mathematically, this is represented by

$$V = -(m\vec{Q}\cdot\vec{G} + M\vec{P}_R\cdot\vec{G} + M\vec{P}_L\cdot\vec{G}) \tag{6.4}$$

However, Eq. (6.4) is complicated by the fact that we wish to examine the vehicle dynamics while traversing an arbitrarily inclined plane. The gravitational field term of Eq. (6.4) needs to be defined in a more rigorous manner. Equations (6.1) and (6.2) suggest the Newtonian fixed frame is coincident with the plane on which the vehicle is in contact. This convention in the kinematic definition has been enforced by design. It is easier to redefine the gravitational field for different planes than it is to redefine the position vectors.

Consider a plane that is rotated using 2-1 Newtonian angles b_x and b_y. It can be shown that we may arbitrarily orient a plane in Newtonian space using only two rotations. The Newtonian cosine direction matrix associated with transforming a general directional reference from the gravity-coincident system to the plane-fixed Newtonian reference is derived as

$$\begin{bmatrix} \hat{g}_1 \\ \hat{g}_2 \\ \hat{g}_3 \end{bmatrix} = \begin{bmatrix} \cos b_x & \sin b_y \sin b_x & -\cos b_y \sin b_x \\ 0 & \cos b_y & \sin b_y \\ \sin b_x & -\sin b_y \cos b_x & \cos b_y \cos b_x \end{bmatrix} \begin{bmatrix} \hat{n}_1 \\ \hat{n}_2 \\ \hat{n}_3 \end{bmatrix} \tag{6.5}$$

In the case of a gravitational field, we only wish to know the rotational components operating on the original *k* direction. Decomposing Eq. (6.5) and applying it to the known gravitation field results in an expression for the local gravitational field in terms of our Newtonian fixed reference coordinates. Since we are concerned with the vehicle on a plane, we can realign the Newtonian reference frame of figure 6.1 such that $\boldsymbol{n_1}$ and $\boldsymbol{n_2}$ lie within the plane of motion. By doing so, the gravitational field as viewed from the Newtonian reference becomes

$$\vec{G} = -g\left[\sin b_x \hat{n}_1 - \sin b_y \cos b_x \hat{n}_2 + \cos b_y \cos b_x \hat{n}_3\right] \tag{6.6}$$

Substituting this result back into Eq. (6.4) completes the energy definitions in the three-dimensional biplanar bicycle system.

6.3 Generalized Forces

Before equations of motion can be developed, we must consider any external generalized forces acting on the system. Like the planar model, we neglect the effects of aerodynamic body forces and focus only on the forces generated by the DC drive motors. Although the input torque generated by the motors has been derived in previous chapters, the model is repeated here for convenience. The torque developed by each motor is defined using the motor torque constant and the armature current.

$$t = K_t i_a \tag{6.7}$$

The armature current is modeled using both the armature resistance and the electrical back EMF constant. In this case, the rotational coordinate in q is for the right and left wheels. One torque equation must be developed for each wheel.

$$i_a = \frac{V_a}{R_a} - \frac{K_B}{R_a}\left(\dot{q} + \dot{f}\right) \tag{6.8}$$

Combining equation (6.7) and (6.8) we develop the final torque equation.

$$t = \frac{K_T}{R_a} V_a - \frac{K_T K_B}{R_a}\left(\dot{q} + \dot{f}\right) = K_1 V_a - K_2\left(\dot{q} + \dot{f}\right) \tag{6.9}$$

At this point the derivation differs in form from that in chapter three. Consider the general definition for calculating generalized forces acting on j generalized coordinates

$$Q_j = \sum_i F_i \cdot \frac{\partial r_A}{\partial q_j} + M_A \cdot \frac{\partial w}{\partial \dot{q}_j} \tag{6.10}$$

where r_A are vectors locating points at which i forces are applied and M_A are moments acting on the bodies rotating at w. From this, we deduce that the force affecting the

reaction mass is no longer a single torque, but rather a linear combination of the torque produced by both drive motors. Implementing Eq. (6.10) and defining motor torques with Eq. (6.9) we calculate the generalized forces acting on each of the generalized coordinates. The resulting forces are

$$\begin{aligned} Q_{q_R} &= K_1 V_{a_R} - K_2\left(\dot{q}_R + \dot{f}\right) \\ Q_{q_L} &= K_1 V_{a_L} - K_2\left(\dot{q}_L + \dot{f}\right) \\ Q_f &= K_1\left(V_{a_R} + V_{a_L}\right) - K_2\left(\dot{q}_R + \dot{q}_L + 2\dot{f}\right) \end{aligned} \tag{6.11}$$

6.4 Dynamic Model

In order to complete the dynamic model, we have to define further kinematic constraints to relate the vehicles spatial position to the motion of the generalized variables. First, there exists a constraint that relates the angular position a of the vehicle and its total time derivatives to the angular positions q_i of the wheels and their total time derivatives. These relationships can be expressed as

$$\begin{aligned} a &= \frac{R\left(q_R - q_L\right)}{2d} \\ \dot{a} &= \frac{R\left(\dot{q}_R - \dot{q}_L\right)}{2d} \\ \ddot{a} &= \frac{R\left(\ddot{q}_R - \ddot{q}_L\right)}{2d} \end{aligned} \tag{6.12}$$

Equation (6.12) is commonly used in the process of vehicular ground navigation by means of dead reckoning. For example, the differential mechanism at the heart of the notorious South pointing chariot is inherently based on the same concepts. However, it is important to note that Eq. (6.12) is derived and proved assuming the vehicle operates in accordance with conditions of no slip. Even though we have shown in chapter four that

this assumption is robust for real vehicles, it remains a kinematic constraint that must be dealt with in any mathematical simulation.

Unlike the planar case in which the no-slip condition can be enforced by equating wheel rotation to linear distance, the same constraint in spatial coordinates creates a non-holonomic constraint between the wheels and the rigid rolling surface. We must therefore ensure proper contact forces under each wheel's no-slip condition so that angular velocity of a wheel remains proportional to its linear velocity. We define the velocities of the wheels to be

$$\begin{aligned} V_R &= \frac{d}{dt}\vec{P}_R = (\dot{x} + \dot{a}\, d\cos a)\hat{n}_1 + (\dot{y} + \dot{a}\, d\sin a)\hat{n}_2 \\ V_L &= \frac{d}{dt}\vec{P}_R = (\dot{x} - \dot{a}\, d\cos a)\hat{n}_1 + (\dot{y} - \dot{a}\, d\sin a)\hat{n}_2 \end{aligned} \tag{6.13}$$

Because Eq. (6.12) already enforces constant distance between the wheel centers (it assumes a non-extensible axle) we need only employ the no slip condition for a single wheel. Examining the similarities between the resulting constraint equations for each wheel can mathematically demonstrate this idea.

$$\begin{aligned} V_R &= (\dot{x} + \dot{a}\, d\cos a)\hat{n}_1 + (\dot{y} + \dot{a}\, d\sin a)\hat{n}_2 = (R\dot{q}_R\cos a)\hat{n}_1 + (R\dot{q}_R\sin a)\hat{n}_2 \\ V_L &= (\dot{x} - \dot{a}\, d\cos a)\hat{n}_1 + (\dot{y} - \dot{a}\, d\sin a)\hat{n}_2 = (R\dot{q}_L\cos a)\hat{n}_1 + (R\dot{q}_L\sin a)\hat{n}_2 \end{aligned} \tag{6.14}$$

We can now separate one of the relationships in Eq. (6.14) into two scalar equations. This yields the two constraint equations with which we enforce the no-slip condition. Using the vector equation for the right wheel only we find the resulting constraints to be

$$\begin{aligned} \dot{x} + \dot{a}\, d\cos a &= R\dot{q}_R\cos a \\ \dot{y} + \dot{a}\, d\sin a &= R\dot{q}_R\sin a \end{aligned} \tag{6.15}$$

Because the constraint equations in Eq. (6.15) have first order terms, it is necessary when applying the Lagrange multipliers that the full variational result is used. Therefore, the

full extended Lagrange equation with Raleigh dissipation is used. C_i denotes one of n_c constraint equations and l_i is the multiplier associated with the constraint. In this case, four Lagrange multipliers are required to fully constrain the system to the non-holonomic no-slip condition.

$$\sum_{i=1}^{n_C}\left[\frac{d}{dt}\left(\frac{\P \mathrm{L}}{\P \dot{q}_j}\right)-\frac{\P \mathrm{L}}{\P q_j}+\frac{\P \mathrm{D}}{\P \dot{q}_j}-l_i\frac{\P C_i}{\P q_j}-\frac{d}{dt}\left(l_i\frac{\P C_i}{\P \dot{q}_j}\right)\right]=Q \tag{6.16}$$

We now have a system of seven coupled differential equations and seven unknown accelerations. However, the two constraint equations (6.15) are functions of the states only. This reduces our set to five equations and seven unknowns. Therefore, before the system may be solved, the total time derivatives of the constraint equations must be taken, remembering that a is a function of q_i. We now have sufficient equations to solve the system. Further, the unknowns in the system are now

$$\ddot{q}_R \quad \ddot{q}_L \quad \ddot{f} \quad \ddot{x} \quad \ddot{y} \quad \dot{l}_1 \quad \dot{l}_2 \tag{6.17}$$

It should be noted that this system is considerably more complicated than the planar model developed in chapter three. To date, the mathematics involved in solving this system are too complicated for most symbolic and numerical solution software packages. Further, the potential payoff in the solution of this system is relatively low and resides primarily in navigation and control of high-speed vehicles. For these reasons, the solution of the three-dimensional system is not completed and left as a topic of future research. The Mathematica code and resulting coupled equations of motion are presented in the Appendix as a resource during future work.

Chapter 7

Orientation-Regulated Platforms for Use in Biplanar Bicycles

The dynamics of the biplanar bicycle have been explored in depth during previous chapters. We have seen both planar and three-dimensional models and have simulated and attempted basic control of the planar system. We have also spent extensive energy in understanding the operational envelops of these vehicles, and have a firm grasp on their salient operational characteristics. However, we have done little beyond heuristic thought experimentation in the consideration of application and usage of this new vehicle class. Some ideas, such as planetary exploration, landmine clearance, and railroad inspection are striking in their potential. Unfortunately, the design challenges associated with implementing this type of vehicle do not cease with the design of the vehicle geometry. Many secondary design considerations must be accounted for prior to the fielding any such ground vehicle. This chapter demonstrates an example of one of these problems.

7.1 The Pendulation Problem

Kinematically speaking, the biplanar bicycle contains no grounded or Newtonian-fixed link within its body-relative system. This can also be restated to say that at no time during operation can we assume to know the direction of the local gravitational field with

respect to vehicle components. In fact, calculating the gravitational direction is made more difficult, especially during transient motion, because we do not know the local terrain slope. the lack of a Newtonian ground prevents our design from having a linkage to maintain directional information. The result of all this is the potentially detrimental pendulation of any and all devices being carried by the vehicle chassis.

One application in which this problem becomes evident is in the implementation of computer vision which is needed in most autonomous robotic applications. Regardless of what kind of camera is being used, its pendulation about the axle predicates the implementation of rigorous mathematics to compute navigation and obstacle avoidance routines. It is possible to nearly counter-balance a camera spar with a passive weight, but the pendulation will continue unless the counter-balance is perfect. Although an attractive prospect, this design fails with the introduction of any exogenous system inputs such as aerodynamic drag or viscous damping in the mount bearing. Any generalized external moment will, during a finite duration of application, force the counterbalanced system into an orientation other than that which is desired. It becomes evident that in order to isolate any peripheral or excitation-sensitive equipment from the vehicle dynamics, a controlled stable platform must be designed. The rest of this chapter develops such a platform and uses the camera spar used in computer vision as a working example. However, the control techniques developed herein are applicable for any platforms.

7.2 Possible Control Techniques

As stated before, one control technique is simple mass counterbalance sufficient enough to maintain the camera's position above the axle. Although the resulting pendulum is stable, the accelerations of the axle result in base-excited oscillations. Further, adjustment of the CG location does not eliminate the problem; in fact the result is a new design trade off. Consider, for modest disturbances, the frequency of the induced nonlinear oscillation is given by (Nayfeh and Mook, 1979)

$$w = \sqrt{\frac{g}{l_{CG}}}\left(1 - \frac{1}{16}a^2\right) + O\left(a^3\right) \tag{7.1}$$

and so a reduction in the distance between the CG and the axle decreases the period of the motion resulting in a faster return to the unperturbed orientation. However, a decrease in l_{CG} results in a reduction in the restoring moment as can be seen by differentiation of the potential energy with respect to the angular coordinate (Meirovitch, 1970):

$$M_{restoring} = \frac{\partial V}{\partial q} = mgl_{cg}\sin q \tag{7.2}$$

Such reductions culminate with zero restoring moment as the mass moves closer to the pivot point even as the frequency of motion approaches infinity (the result is marginal stability; perturbations result in unrecoverable deviations). Having seen the inadequacy of the counter-balance, the next logical step in system control would be to implement a simple open-loop control strategy in which employ an equal and opposite rotation with respect to the wheels. This would certainly result in a fixed camera orientation. However, this approach relies completely on dead reckoning and may therefore fall short as a robust control strategy. The only alternative remaining is the implementation of an active control technique.

In considering any active control, one must reconsider the lack of fixed ground from which to react any control efforts. Two mass-based control alternatives exist. Used in space applications for similar reasons, thrusters and reaction masses are employed to impart forces on structures. Although either would prove sufficient, the reaction mass is more appropriate to ground-based vehicle architecture. Here, a secondary ballast is employed in a double pendulum arrangement. Actively controlling the angle between the bottom pendulum relative to the upper pendulum with a simple DC servomotor provides the inertial and gravitational resistance necessary to generate the control torque.

Although this control solution adds otherwise passive mass to the vehicle, it seems to stand out as the most attractive alternative.

7.3 Dynamic Model

A rigid-body dynamic model of the system shown in Fig. 7.1 can be easily developed based on complex-vector (planar) kinematics and Hamiltonian dynamics.

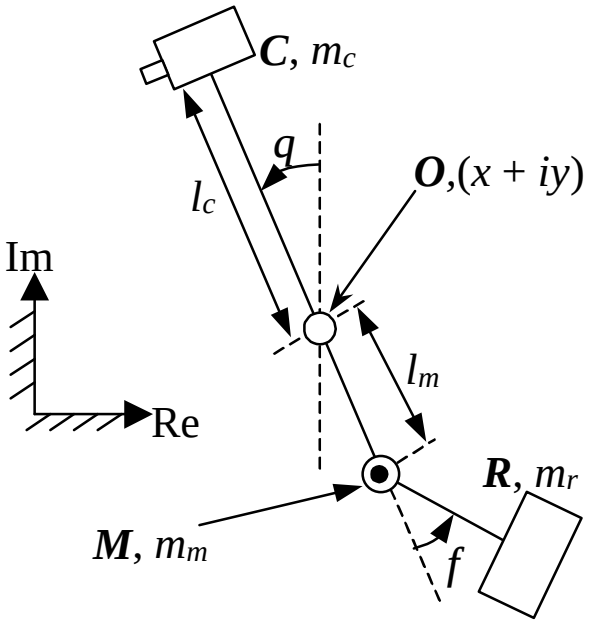

Figure 7.1: Kinematic Diagram for Camera Stabilization

Establishing a fixed reference frame in the plane of action of the system, with the gravitation force orientated in the negative imaginary direction, the locations of the axle, the control motor, the reacting mass, and the camera are given by

$$\vec{O} = \hat{x}(t) + j\hat{y}(t) \tag{7.3}$$

$$\vec{M} = \vec{O} - jl_m e^{jq(t)} \tag{7.4}$$

$$\vec{R} = \vec{M} - jl_r e^{j(q(t)+f(t))} \tag{7.5}$$

$$\vec{C} = \vec{O} + jl_c e^{jq(t)} \tag{7.6}$$

With the system geometry defined, we can now define the system kinetic and potential energy. The resulting energy equations are

$$T = \frac{1}{2}\left[m_c \dot{\vec{C}} \cdot \dot{\vec{C}} + m_m \dot{\vec{M}} \cdot \dot{\vec{M}} + m_r \dot{\vec{R}} \cdot \dot{\vec{R}}\right] \tag{7.7}$$

$$V = g\left[m_c \vec{C} \cdot j + m_m \vec{M} \cdot j + m_r \vec{R} \cdot j\right] \tag{7.8}$$

Again, we wish to maintain a level of physical relevance and add a Rayleigh dissipation function to account for what is modeled as linear viscous damping in the joint bearing. The primary advantage of this is to ensure all system poles do not lie on the imaginary axis. This is desirable since losses in any real system prohibit marginal dynamic stability. The desired function is

$$R = \frac{1}{2} c \dot{q}^2 \tag{7.9}$$

The equations of motion are then found by the application of the extended Lagrange equations

$$\frac{d}{dt}\left(\frac{\partial T}{\partial \dot{q}_j}\right) - \frac{\partial T}{\partial q_j} + \frac{\partial V}{\partial q_j} + \frac{\partial R}{\partial \dot{q}_j} = Q_j \tag{7.10}$$

where $q = (q, f)$ and $Q = (0, t)$ where t is the controller motor torque. In the servo-dynamic model the back EMF and armature resistance are considered while the motor inductance is neglected. The equation that governs the torque output verses the applied voltage is given by

$$t = \frac{K_T}{R_a} v_a - \frac{K_B K_T}{R_a} \dot{f} \tag{7.11}$$

To increase the utility of the equations for design and analysis, the following nondimensional parameters and variables are introduced

$$L_m = \frac{l_m}{l_c} \qquad L_r = \frac{l_r}{l_c} \qquad M_m = \frac{m_m}{m_c} \qquad M_r = \frac{m_r}{m_c}$$

$$z = \frac{c}{l_c^2 m_c w_c} \qquad x = \frac{K_T K_B}{R_a l_c^2 m_c w_c^2} \qquad v = \frac{K_T \hat{v}}{R_a l_c^2 m_c w_c^2}$$

$$x = \frac{\hat{x}}{l_c} \qquad y = \frac{\hat{y}}{l_c} \qquad t = \hat{t} w_c$$

where $w_c = \sqrt{g / l_c}$ and "^" denotes a dimensional variable.

The result of expressing the equations of motion obtained from Eqs. (7.10) and (7.11) in terms of the nondimesionalized parameters and variables is

$$\begin{aligned} &(m_1 + m_2 + 2m_3 \cos f)\ddot{q} + (m_2 + m_3 \cos f)\ddot{f} + \\ &\quad (z - 2m_3 \dot{f} \sin f)\dot{q} - m_3 \dot{f}^2 \sin f + \\ &\quad [k_1 \sin q + k_2 \sin(q + f)](1 + \ddot{y}) \\ &\quad = [-k_1 \cos q - k_2 \cos(q + f)]\ddot{x} \end{aligned} \tag{7.12}$$

and

$$\begin{aligned} &(m_2 + m_3 \cos f)\ddot{q} + m_2 \ddot{f} + m_{3r} \dot{q}^2 \sin f + x\dot{f} + \\ &\quad k_2 \sin(q + f)(1 + \ddot{y}) = -\cos(q + f)\ddot{x} + v \end{aligned} \tag{7.13}$$

where

$$
\begin{aligned}
m_1 &= 1 + L_m^2 (M_m + M_r) \\
k_1 &= L_m (M_m + M_r) - 1 \\
m_2 &= L_r^2 M_r \\
m_3 &= L_m L_r M_r \\
k_2 &= L_r M_r
\end{aligned}
\tag{7.14}
$$

and overdots now indicate differentiation with respect to non-dimensional time.

7.4 Controller Design

In the design of an active feedback controller, we take advantage of the relatively generous region of near-linear behavior of pendulums for moderate angular deflections. Because the temporal character of the disturbance excitation is not known *a priori*, we attack the problem as a simple regulation of the equilibrium. By designing a full-state-feedback regulator for the system, the closed-loop robustness to external forcing is improved by the increase in effective linear damping.

Here, we seek to design a fixed gain, linear, state feedback controller using the techniques of optimal control. The basis for the control-law design is the linearization of the plant via a power series expansion in f and q about the trivial equilibrium point. Next, a Linear Quadratic Regulator (LQR) controller is designed to minimize the (quadratic) cost functional based on the linear approximation to the plant.

Upon linearization the equations are transformed to state-space form to allow the tools of modern controls be applied. The form of the state space equation is

$$
\dot{\mathbf{x}} = \mathbf{A}\mathbf{x} + \mathbf{b}v \tag{7.15}
$$

The state vector **x** is established as $\begin{bmatrix} q & f & \dot{q} & \dot{f} \end{bmatrix}^T$. The state matrix **A** is developed based on the mass, damping, and stiffness matrices associated with the linearization:

$$\mathbf{A} = \begin{pmatrix} \mathbf{0} & \mathbf{I} \\ -\mathbf{M}^{-1}\mathbf{K} & -\mathbf{M}^{-1}\mathbf{C} \end{pmatrix} \tag{7.16}$$

where

$$\begin{gathered} \mathbf{M} = \begin{pmatrix} m_1 + m_2 + 2m_3 & m_2 + m_3 \\ m_2 + m_3 & m_2 \end{pmatrix} \\ \mathbf{C} = \begin{pmatrix} z & 0 \\ 0 & x \end{pmatrix} \quad \text{and} \quad \mathbf{K} = \begin{pmatrix} k_1 + k_2 & k_2 \\ k_2 & k_2 \end{pmatrix} \end{gathered} \tag{7.17}$$

The input vector **b** is given by

$$\mathbf{b} = \begin{pmatrix} \mathbf{0} \\ \mathbf{M}^{-1}\mathbf{u} \end{pmatrix} \tag{7.18}$$

where $\mathbf{u}^T = \begin{pmatrix} 0 & 1 \end{pmatrix}$. We seek to apply a state-feedback control law:

$$\begin{gathered} v = -\mathbf{g}^T \mathbf{x} \\ \dot{\mathbf{x}} = \mathbf{A}\mathbf{x} - \mathbf{b}\mathbf{g}^T \mathbf{x} = \left(\mathbf{A} - \mathbf{b}\mathbf{g}^T\right)\mathbf{x} \end{gathered} \tag{7.19}$$

where the design of $\mathbf{g}^T$, the feedback-gain row vector, is the essential control problem. The performance index for the infinite-time-horizon LQR controller is defined as

$$J = \int_0^\infty \left(\mathbf{x}^T \mathbf{Q}\mathbf{x} + rv^2\right) dt \tag{7.20}$$

where **Q** and r are weighting factors associated with response and control effort, respectively (Zhou, Doyle, Glover, 1996). The optimizing control using this performance index satisfies the algebraic Riccati equation

$$\mathbf{PA} - \frac{1}{r}\mathbf{Pbb}^T\mathbf{P} + \mathbf{A}^T\mathbf{P} + \mathbf{Q} = \mathbf{0} \tag{7.21}$$

where

$$\mathbf{g}^T = -\frac{1}{r}\mathbf{b}^T\mathbf{P}$$

P may be determined using Potter's algorithm (Meirovitch, 1989).

7.5 Numerical Simulations

Applying the above control law, the closed-loop system was simulated via numerical simulation. The values for the non-dimensional parameters used in the simulation were

$K_m = 2$ $M_m = 3$ $M_r = 4$

$L_m = 1/6$ $L_r = 1/6$ $z = 0.2$ $w_c = 3.27$ rad/s

The weighting factors used in the LQR cost functional

$$\mathbf{Q} = \text{diag}[10000 \quad 100 \quad 0 \quad 0] \text{ and } r = 1$$

(note that Q is positive semi-definite) results in the state feedback gain vector

K = [92.06 6.84 –49.14 –6.96].

The closed-loop system robustness is demonstrated by considering initial condition responses and horizontally and vertically forced responses. For example, Fig. 7.2a demonstrates the system's fast decay rate when subjected to an initial displacement of 10^o. The associated control effort is shown in Fig. 7.2b as $f(t)$.

Figure 7.3a demonstrates system response to base disturbances of $\ddot{y} = 0.1\sin t$ and $\ddot{x} = 0.1\cos t$. After a short transient, the system stabilizes in a 2^o sinusoidal oscillation.

The control effort associated with this base excitation is shown as $f(t)$ in Fig. 7.3b. It is clear from the simulations that the controller adequately maintains a stable platform. Again, this example is arbitrary in the choice of LQR weighting matrices. The designer should reconsider the numerical values used in this process for application-specific designs but can maintain the general design methods if total success is expected.

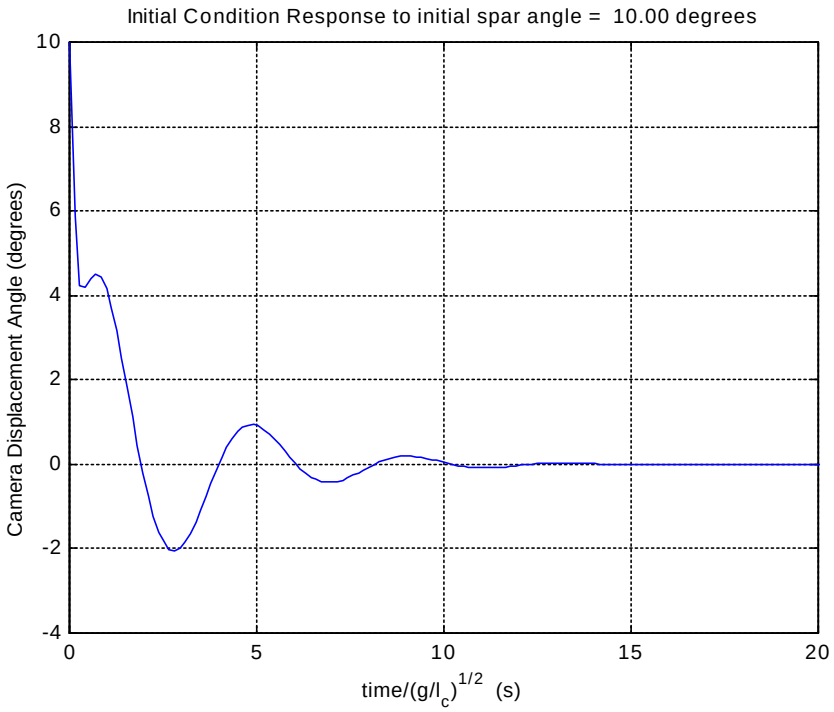

Figure 7.2a: Controlled response to an initial condition displacement of the camera spar

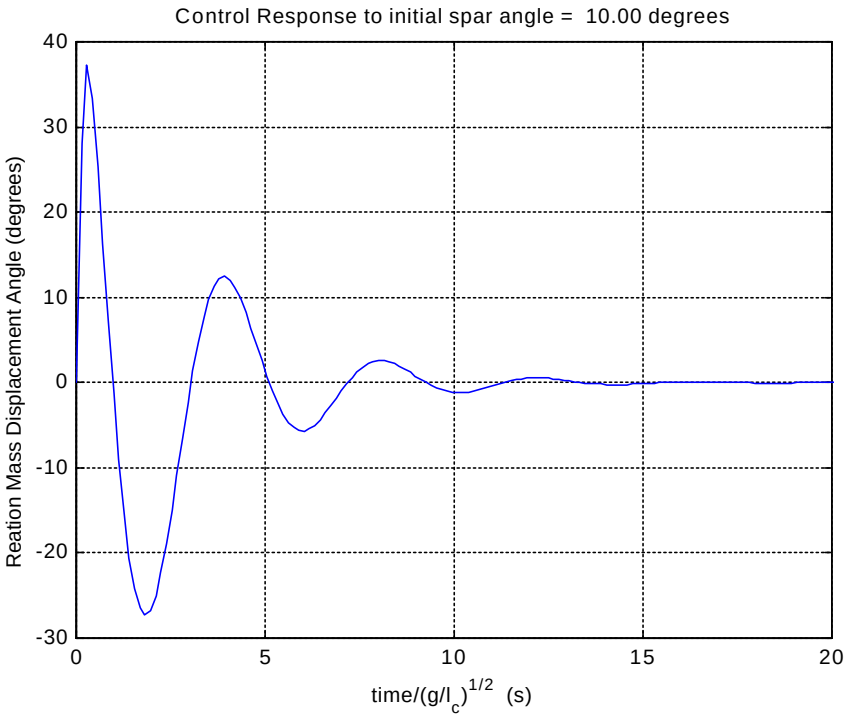

Figure 7.2b: Control effort in reaction mass to an initial condition displacement

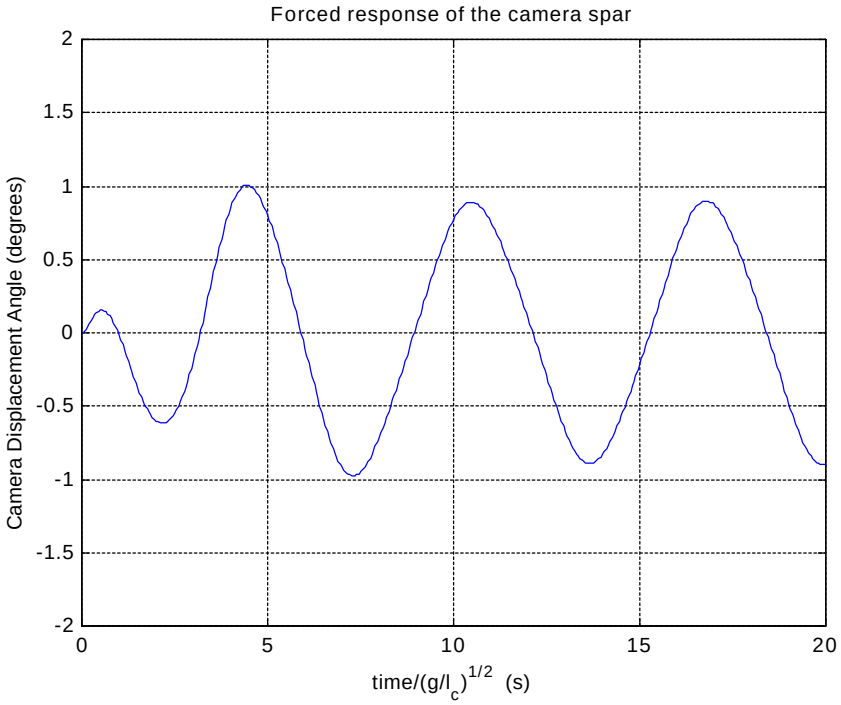

Figure 7.3a: Camera displacement for the forced system

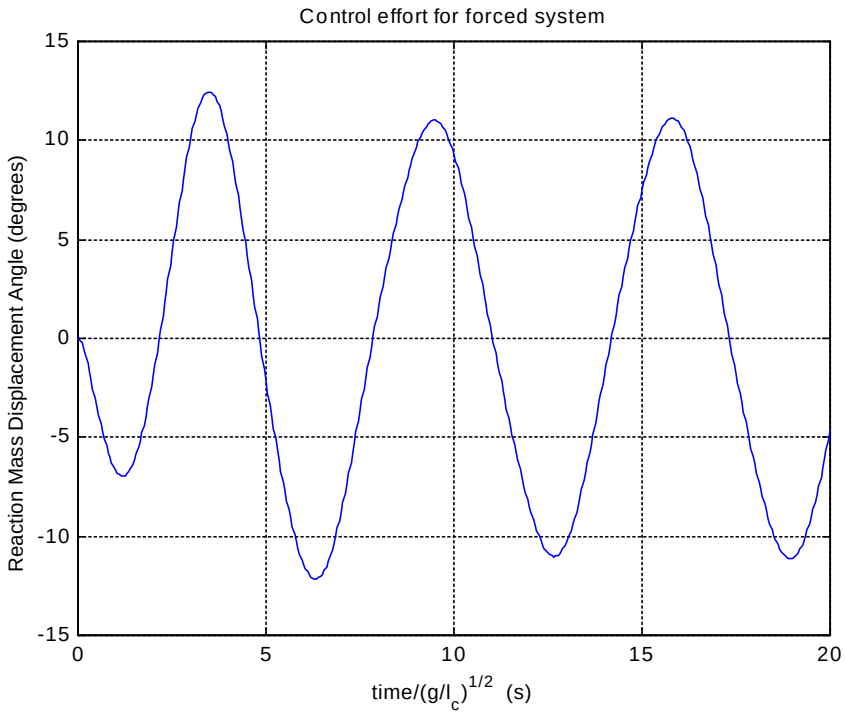

Figure 7.3b: Control effort for the forced system

Chapter 8

Coupled Vehicle-Camera Dynamics and Control

The platform stabilization routine in chapter seven was purposefully developed to act independently of the vehicle dynamics. We have demonstrated the controller's ability to reject base excitations and maintain a reasonably constant camera angle. However, it would still be a prudent exercise to investigate the coupled dynamics of the platform and vehicle systems. Even though the vehicle does not change the controller dynamics, the existance of the the platform and associated reaction mass will change the vehicle performance. In this chapter, we focus on the performance effects of coupling the two systems and then suggest alternative designs that may provide advantages over the currently proposed design.

8.1 Dynamic Model

We begin by using the camera spar as the example platform and redefine the kinematics of the combined system. As can be seen in figure 8.1, the total system now contains four generalized coordinates, two from each of the independent systems.

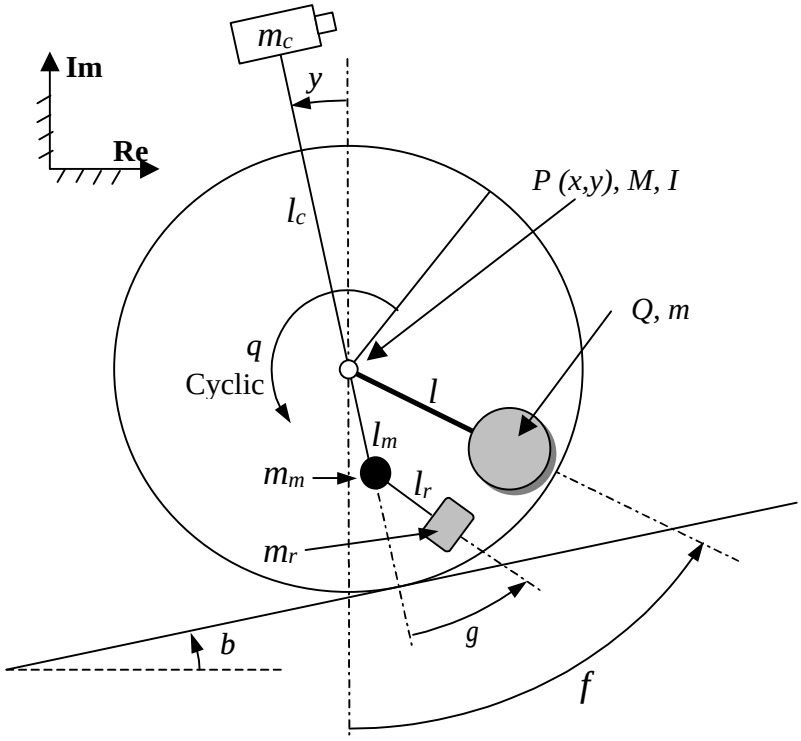

Figure 8.1: Coupled Vehicle-Camera Kinematic Definitions

No changes have been made from the vehicle nomenclature presented in chapter three. However, some new variables had to be added to the camera system from chapter seven. The angles associated with camera and reaction mass motion have been renamed to avoid redundancy. Further, the system will ultimately be non-dimensionalized with respect to the wheel radius r and mass M. Finally, reference for wheel rotation angle q is simply suggested in figure 8.1 but is assumed to lie along the imaginary axis at time $t = 0$. We may do so without loss of generality because of the cyclic nature of the variable as discussed in chapter three.

In superimposing the systems, we may write the system kinetic and potential energies as the linear combination of those developed earlier. Likewise, the Rayleigh dissipation functions may also be combined. All these are repeated and combined here with the modified coordinate nomenclature.

$$T = \frac{1}{2}\left[m\dot{\vec{Q}} \cdot \dot{\vec{Q}} + \frac{1}{2} M\dot{\vec{P}} \cdot \dot{\vec{P}} + m_c \dot{\vec{C}} \cdot \dot{\vec{C}} + m_m \dot{\vec{M}} \cdot \dot{\vec{M}} + m_r \dot{\vec{R}} \cdot \dot{\vec{R}} \right] + \frac{1}{2} I\dot{q}^2 \tag{8.1}$$

$$V = mg\left(\vec{Q} \cdot j\right) + Mg\left(\vec{P} \cdot j\right) + m_c g\left(\vec{C} \cdot j\right) + m_m g\left(\vec{M} \cdot j\right) + m_r g\left(\vec{R} \cdot j\right) \tag{8.2}$$

$$R = \frac{1}{2} C\left(\dot{q} + \dot{f}\right)^2 + \frac{1}{2} C\dot{y}^2 \tag{8.3}$$

With *T*, *V*, and *R* defined we may now solve the extended Lagrange equation for the dynamic response. This is represented as

$$\frac{d}{dt}\left(\frac{\P T}{\P \dot{q}_j} \right) - \frac{\P T}{\P q_j} + \frac{\P V}{\P q_j} + \frac{\P R}{\P \dot{q}_j} = Q_j \tag{8.3}$$

where $q = (q, f, y, g)$ and $Q_j = (t, t, 0, t)$. To maintain consistency between the models presented in chapters three and seven, the motor torques t are defined with identical motor constants. The DC servomotor model developed earlier remains the same and the resulting expression for motor torque on both drive and control motors is shown to be

$$t = \frac{K_T}{R_a}\hat{V}_a - \frac{K_B K_T}{R_a}\left(\dot{q} + \dot{f}\right) \tag{8.4}$$

As we have done in all past models, the system is simplified by introducing non-dimensional variables and parameters. Because the vehicle is of primary concern we will maintain the wheel radius and mass as the characteristic length and mass. By doing so, the parameters and variables defined in chapter seven are rendered invalid, as they are now in terms of a vehicle dimension. Also note the addition of two new parameters to describe the camera spar length and camera mass. We introduce the non-dimensional parameters

$$L=\frac{l}{r} \qquad L_m=\frac{l_m}{r} \qquad L_p=\frac{l_p}{r} \qquad L_r=\frac{l_r}{r}$$

$$a=\frac{m}{M+m} \qquad M_m=\frac{m_m}{M} \qquad M_r=\frac{m_r}{M} \qquad M_c=\frac{m_c}{M} \tag{8.5}$$

$$z=\frac{C}{r^2 w}+\frac{K_B K_T}{R_a r^2 (M+m) w} \qquad m=\frac{I}{(M+m) r^2}$$

and variables

$$U=\frac{K_T \hat{V}_a}{R_a r^2 (M+m) w^2}, \quad v=\frac{K_T \hat{v}}{R_a l_c^2 m_c w_c^2} \quad \text{and} \quad \mathrm{t}=\hat{t} w \tag{8.6}$$

where $w=\sqrt{g/r}$. Once again we take advantage of the relatively generous region of near-linear behavior of pendulums for moderate angular deflections. As before, the temporal character of the disturbance excitation is not known *a priori*. However, we designed the previous full-state feedback regulator without any regard to the disturbance source. Therefore, it would be a logical assumption that the regulator design should remain unchanged by the addition of the vehicle. Mathematically, we see a difference in the system dynamic matrices caused by the change in source description. We no longer describe the base excitation with a arbitrary *x* and *y* motion but rather incorporate the motion at point *P* based on the vehicle coordinates q and f. Using the same process of power expansion and LQR design presented in chapter seven we linearize the camera system about the trivial solution. In doing so we may see the new mass, stiffness, and damping matrices to be

$$M=\begin{bmatrix} L_P^2 M_C+L_M^2 M_M+L_M^2 M_R+L_R^2 M_R+2L_M L_R M_R & L_M L_R M_R+L_R^2 M_R \\ L_M L_R M_R+L_R^2 M_R & L_R^2 M_R \end{bmatrix}$$

$$K=\begin{bmatrix} -L_P M_C+L_M M_M+L_M M_R+L_R M_R & L_R M_R \\ L_R M_R & L_R M_R \end{bmatrix} \tag{8.7}$$

$$C = \begin{bmatrix} V & 0 \\ 0 & K \end{bmatrix}$$

As we expected, the LQR controller design produces the same optimal gains for the same relative input parameters. Since the controller design has already been discussed in great detail, we will focus on how the system coupling affects both stabilization and vehicle performance. In order to qualify the results in an easily understood manner, we will discuss performance of both to a step input to the drive motor.

8.2 Simulations of the Coupled System

We have discussed before that we expect no change in camera stabilization performance. As we see in figure 8.2, our insight proves to be accurate.

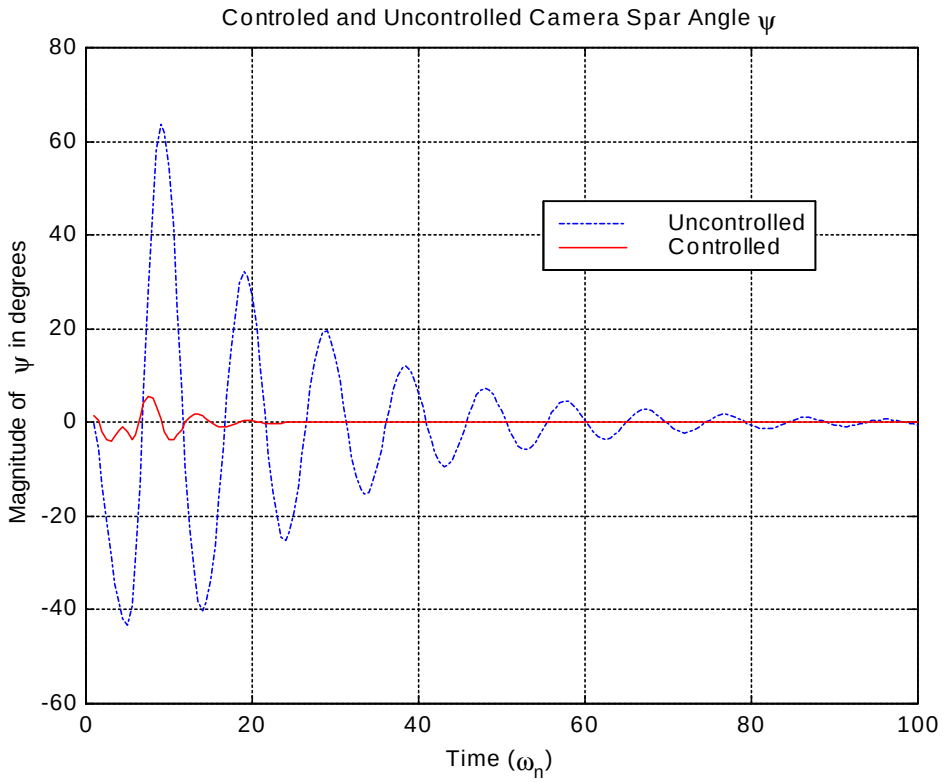

Figure 8.2: Result of Camera Spar Controller in the Coupled System

Using the same relative link lengths, masses, and control gains as found in chapter seven, we see the camera spar is controlled to a maximum angular deviation of approximately 4 degrees. When compared to the uncontrolled deviation of more than 60 degrees, we determine the controller is performing as expected. Additionally, we see the expected linear damping effects of the feedback.

Of course, it is also helpful to determine the control effort involved in accomplishing these results. Figure 8.3 presents the absolute angle of the controller reaction mass.

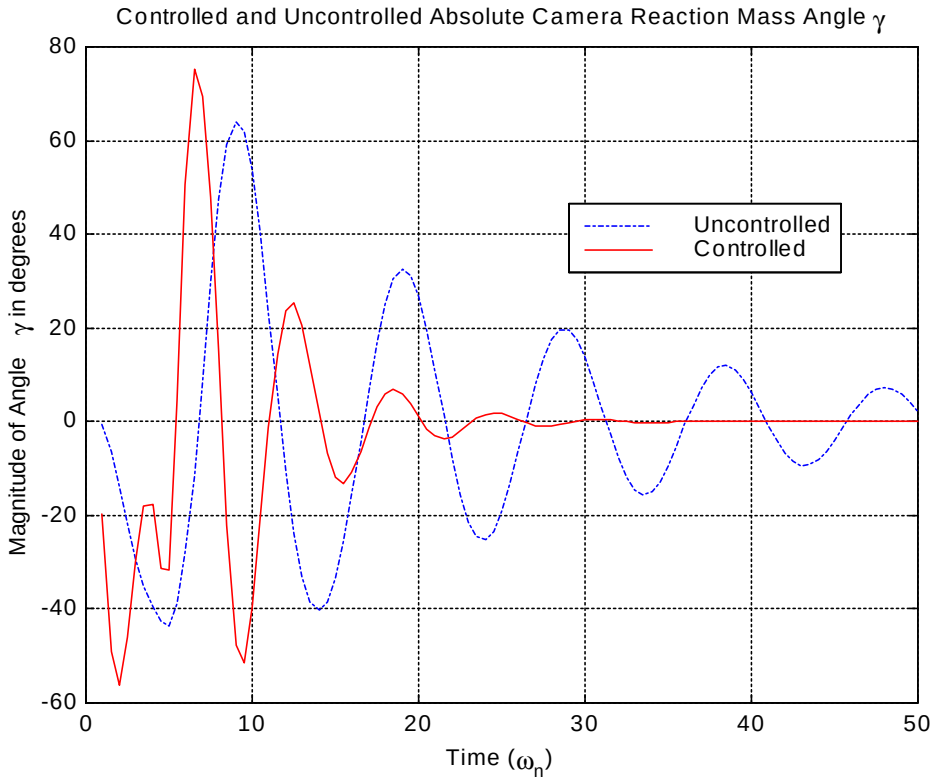

Figure 8.3: Control Effort in Reaction Mass Degrees for a Vehicular Step Input

Recall the reaction mass angle is measured relative to the projected camera spar. Here, the angle is presented as an absolute measurement from the negative imaginary axis to help the reader visualize the system in action. It is interesting to note that the maximum angular displacement of the controlled system is not substatially greater than that of the uncontrolled counterpart.

Again, the results of the controller performance simulations are in no way surprising since the original regulator was designed to reject base-excitation disturbances regardless of input waveform. However, what may not be intuitive in any way are the effects in vehicle performance characteristics. One would probably conclude from intuition that the vehicle will respond substantially differently as a result of mounting the controlled camera system to the axle. However, as is true with many aspects of this new vehicle class, intuition would prove incorrect in this case.

8.3 Coupled System Stability

If we re-examine stability characteristics as we did in chapter three, we see the static and dynamic equilibrium conditions remain identical in nature; they simple have added mass terms. First, consider again the equilibrium solution in which the vehicle remains static on an arbitrarily inclined plane. The resulting conditions for static equilibrium are

$$\left(1+M_C+M_M+M_R\right)\sin\left(b\right)=U_o \quad \text{and} \quad La\,\sin\left(f_o\right)=U_o \tag{8.8}$$

This result is analogous to the result found in Eq. (3.14). In fact, the only difference between the two is the addition of the camera system masses. The unity term in the mass is the non-dimensional representation of the wheel mass and existed implicitly in the conditions of Eq. (3.14). The relationship correlating the pendulum angle f to the control voltage U_o remains unchanged. Buried in Eq. (8.8) is an expression for the maximum slope on which the biplanar bicycle may rest statically. By using the same logic as we did in chapter three in which we denied the existence of complex angles in f and b we see the maximum slope to be bounded above and below by

$$-\sin^{-1}\left(\frac{La}{1+M_C+M_M+M_R}\right)\le b\le\sin^{-1}\left(\frac{La}{1+M_C+M_M+M_R}\right) \tag{8.9}$$

Since the static equilibrium is based solely on a torque balance between the body mass and reaction mass, the result of Eq. (8.9) seems a logical result. It is important to note,

however, that the control of f by the propulsive drive-motor has no effect on the two new generalized coordinates y and g. In steady state, the camera-system center of mass necessarily has to lie on the same vertical axis as the vehicle axle. Regardless of the controlled angle g, the system will pendulate to its natural equilibrium. This can be shown mathematically in the static equilibrium solutions of the controller's generalized coordinates.

$$y = \sin^{-1}\left(\frac{\hat{v}(t)}{L_p M_c - L_m M_m - L_m M_r}\right) \tag{8.10}$$

$$g(t) = \sin^{-1}\left(\frac{\hat{v}(t)}{L_r M_r}\right) - y \tag{8.11}$$

Once again, it is easily seen that Eqs.(8.10) and (8.11) represent nothing more than a torque balance on the stabilization components. Further, these relationships do not change for the steady-state vehicle velocity equilibrium case.

We can deduce from the stability analysis that the vehicle acts very much like the original uncoupled system when in its steady-state configurations. To determine if any transient differences exist, we turn to numerical simulations. It stands to reason that if we wish to compare the coupled and uncoupled system responses, we should examine both simultaneously under the same input conditions. To do so we apply a step input to the vehicle drive motor in both cases and then apply the controlled camera system to the coupled simulation. The coordinates of interest are those associated with the vehicle performance, q and f. Figure 8.4 presents the wheel rotation angle q for both the uncoupled and controlled-coupled dynamic configurations.

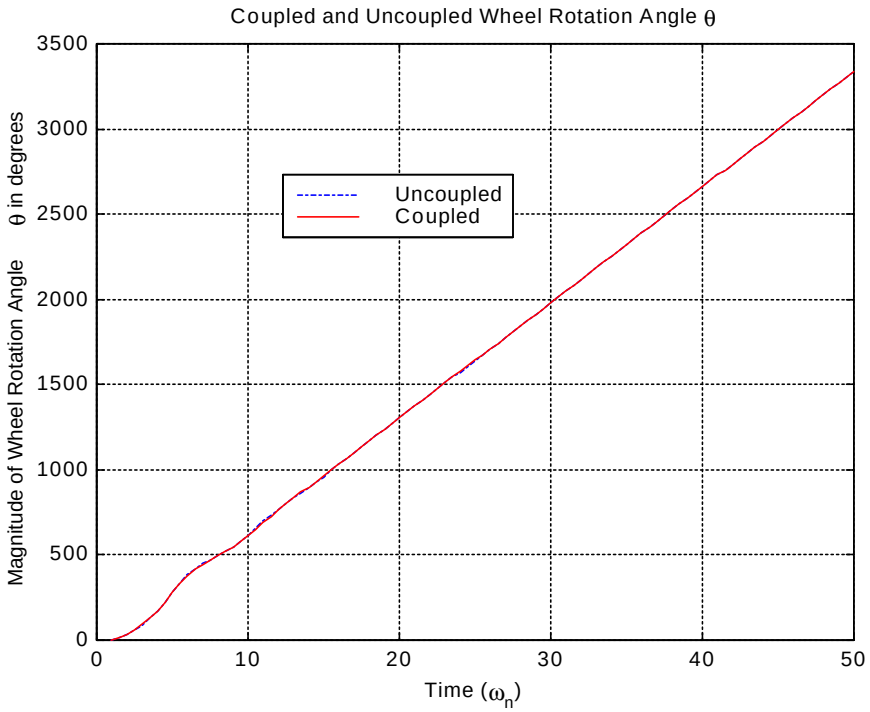

Figure 8.4: Comparison of Uncoupled and Controlled-Coupled Wheel Rotation

It is very apparent that the performace in hill climbing is near identical between the two systems. It would therefore stand to reason that the pendulation angle of the reaction mass should also be very similar for the two cases. Figure 8.5 represents this result.

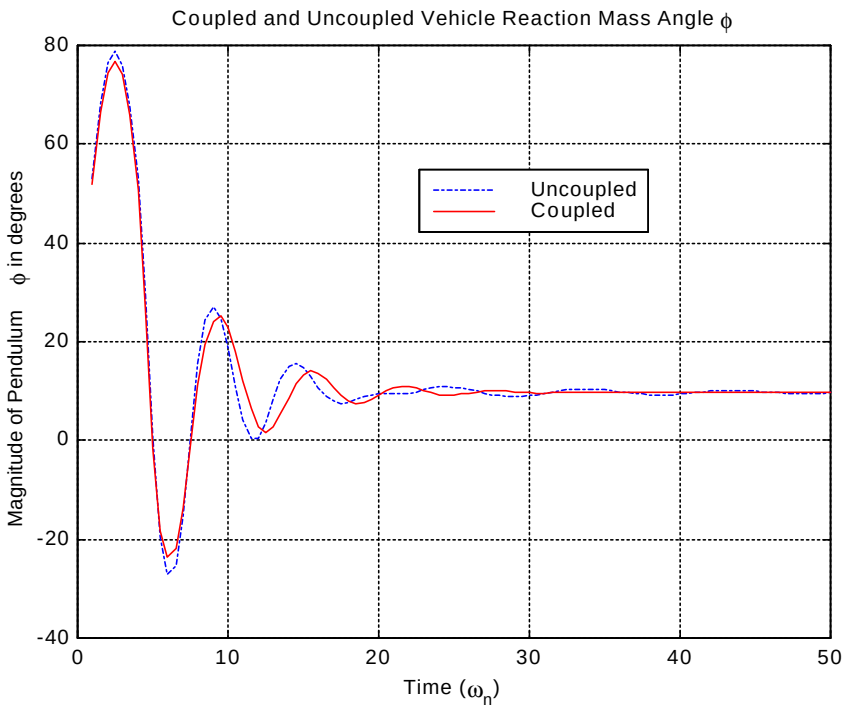

Figure 8.5: Comparison of Uncoupled and Controlled-Coupled Reaction Mass Angle

Indeed, we see the reaction mass performance to be near identical to that of the uncoupled case. More interestingly, figures 8.4 and 8.5 are representative of the system while experiencing input voltages near the critical whirling input. Therfore, what we see here is the near worst-case comparison.

8.4 Results and Further Considerations

Surprisingly, the results of this study suggest that adding a platform stabilization system with a reaction mass as large as 15% that of the vehicle mass does not affect the vehicle performace curves in a significant way. Therefore, the control strategies and performace envelopes developed in previous chapters will still apply in the case of the coupled system design. However, it would also be prudent to consider other design issues associated with coupling these two systems. For example, in order to stabilize a platform in the manner presented here, we necessarily must add additional mass to the overall vehicular system. In applications such as planetary exploration and autonomous ground vehicles where weight-saving is a major driving force, this additional reaction mass may be more detrimental in the end. Several methods of countering this problem are

presented here as food for thought. The development of dynamics and control for these cases is left as an exercise for future research.

If the primary concern with platform stabilization is weight addition, it would only seen reasonable to use the already existing vehicle reaction mass as the stabilization mass. For example, figure 8.6 presents a concept whereby the platform is actuated against the reaction mass via a four-bar linkage.

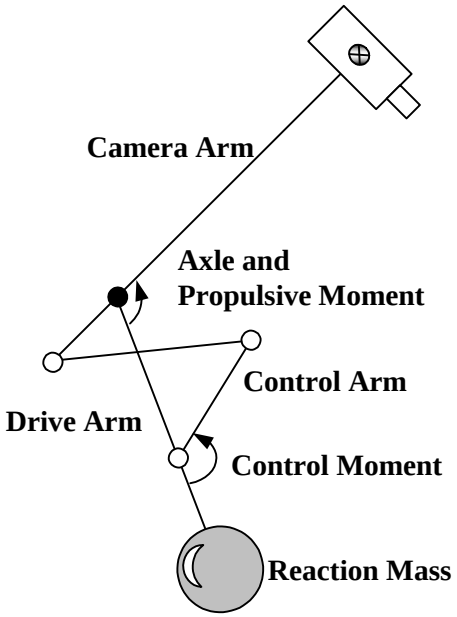

Figure 8.6: Four-Bar Camera Stabilization Concept

The link lengths of the driving four-bar must be designed according to Grashoff's law such that the pendulum link can rotate fully with respect to the camera arm. This way, camera-ground impingement may be avoided during whirling. However, using linkages of this type present issues associated with the kinematics of the drive. Singular positions in the four-bar motion will require instantaneous changes in drive direction in the event of reaction mass whirling. The forces and responses times resulting from such a singular point may prove detrimental to an otherwise robust control strategy.

Another similar drive mechanism is presented in figure 8.7 in which motion is transmitted though linear rather than rotary actuation.

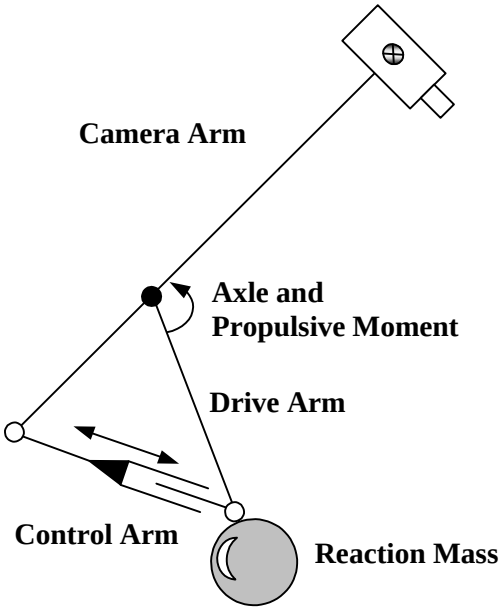

Figure 8.7: Linear Actuated Platform Control Concept

There are obvious limitations to this concept. The control arm must be pinned to the camera spar with an offset. The case of static equilibrium on no grade dictates the colinearity of the camera and drive arms. This would in turn require the control arm to assume a zero-length position. Further, though must be given to what may occur when the reaction mass swings in the negative direction. In spite of these obvious drawbacks, this concept should not be entirely dismissed for low-speed applications in which the vehicle reaction mass angle f is expected to remain relatively small.

It is important to note that the solutions presented here are not intended to cover all possible design solutions to the platform stabilization problem. In fact, we assume many application-specific solutions exist. What has been presented here are the ideas considered from a very general perspective and the solution to one of the simplest configurations conceived to date. However, since the biplanar bicycle is novel in design and application, the designer must remain open to innovative kinematic and control configurations when trying to meet a specific mission.

Chapter 9

Conclusions and Recommendations for Future Work

This work has outlined a foundation of mathematics, analytical methods, and design strategies necessary to complete the robust and reliable design for any biplanar bicycle application. Although the mathematics and simulations presented herein can prove useful in their extension to mission-specific vehicles, they are really intended to provide a solid background in the vehicle class from which the designer may cultivate an intuitive understanding of generalized performance and control characteristics. Understanding the nature of what has been done here is essential in any future development of the biplanar bicycle. Having said this, we can now consider some of the natural spin-offs of this research that must be considered in any future development efforts.

9.1 Future Work

The dynamics for the three-dimensional vehicle have been presented but not solved. At this time, the symbolic representations of the resulting equations of motion are beyond the computing power available. However, the solutions to the dynamics, symbolic or numerical, should be investigated in terms of ground navigation. Until then, dead reckoning seems the logical algorithmic choice for the autonomous ground vehicle applications currently under consideration. Although dead reckoning is a widely

accepted method of navigation, we may find the integration of global positioning to be better suited to some vehicle applications. In the event GPS is desired, navigation no longer stands as the major design challenge. Instead, a deeper understanding of the three-dimensional dynamics will be needed in the planning and control of specific trajectories over known terrain. Careful navigational control schemes may prove beneficial as a means of reducing control effort, minimizing energy dissipation, governing travel time, and controlling obstacle avoidance. Therefore, it stands to reason that as the technology involved in the building and implementation of the biplanar bicycle increases, our ability to analytically model and predict system behavior will become more important. In fact, the three-dimensional dynamic model may one day supercede the planar system presented here as the backbone of vehicular design methodology.

Another focus of future work is experimental validation of the biplanar bicycle's ability to traverse discontinuous terrain. We have suggested the biplanar bicycle may provide distinct advantages in stair climbing. To date we have only verified this concept through calculations and prototype testing. A more rigorous investigation may be prudent if application warrants this capability. As a natural extension of the validation process the generation of performance envelopes based on the relative size of terrain discontinuities would be prudent. This kind of information would be useful not only during the design phase but may also be integrated into the navigational obstacle avoidance algorithms. No everything must be avoided, some things can be climbed and conquered.

In general, we must continue to find and prove the application worthiness of the biplanar bicycle vehicle class. We have learned enough to believe the class provides advantages over classical ground vehicle designs. However, it will never be accepted as a viable solution until we can prove its performance and applicability using prototypes. Therefore, it would be very useful if future researchers choose reasonable applications such as planetary exploration, landmine clearance, and railway inspection and build vehicles capable of completing the tasks as well or better than traditional designs. To this end, the development of an autonomous railway inspection vehicle is suggested as a primary target for vehicle application. Because rail systems naturally constrain the

vehicle in its directional navigation, the planar models presented in this work can be very easily extended to this application. Few issues like non-holonomic constraints and added kinematics would arise in this design. Therefore, we suggest this field as the first likely source of application.

Another very interesting field of work surrounds to continuation of control algorithms for the stabilized platform concept. For example, the four-bar drive linkage concept presented in chapter eight requires the development of a non-learning adaptive control scheme based in system linearization around the constant forward velocity equilibrium points. Using such techniques is the only way the linkage approach would work throughout the vehicle's performance envelope. Further, the non-linear control of the vehicle itself could potentially be improved by implementing the same type of adaptive control strategy. By doing so, the analytical performance envelop information regarding dynamic bifurcation points may be included in the control system design as a way of making the system considerably more robust and reliable with respect to vehicle whirling.

Finally, work must be completed on the physical design of the vehicle. Many ideas concerning the physical realization of a useful vehicle have been considered during this research. Moving all body mass components into the wheel rims would be a method of increasing ground clearance. Adding hemispherical hubs to the drive wheels would allow the vehicle to self-right itself if dropped from aircraft or spacecraft. This idea can be take one step further by designing an extendable axle so the entire vehicle can be deployed as a sphere. Another type of performance improvement involves using more than one point of contact during the traversal of discontinuous terrain as a kinematic ground. By doing so, other internal linkages could be implemented to enhance performance in stair or rock climbing applications.

9.2 Conclusions

The research presented in this work has convinced us that the biplanar bicycle is a viable option in the design of autonomous ground vehicles. We have seen the dynamic

performance, though complicated and at times non-intuitive, are by no means intractable or uncontrollable. We have also shown that some of the more significant issues with the biplanar bicycle concept such as platform stabilization as easily countered with modern control and design techniques. We hope that sometime in the future, this little runt of the ground-vehicle family will find its niche, perform, and succeed in ways that will astound and intrigue engineers and others to the same extent as its more common cousins. We believe it has already made a good start.

REFERENCES

1. Abbott, M. S., Soper, R. R., Grove, D. E., and Reinholtz, C. F.,1999, "Planar Dynamics and Control of a Two-Wheeled Single-Axle Vehicle," *Proceedings of the 1999 ASME International Mechanical Engineering Congress and Exposition*, Nashville, TN. Nov.

2. Avallone, Eugene A., and Baumeister III, T., 1987, *Marks' Standard Handbook for Mechanical Engineers* 9th edition, McGraw-Hill, New York

3. Chen, M. W., and Zalzalsa, A. M. S. , 1997, "Dynamic Modeling and Genetic-Based Trajectory Generation for Non-Holonomic Mobile Manipulators," *Control Engineering Practice*, Vol. 5, No. 1, January, pp. 49-59.

4. James, P., and Thorpe, N., 1994, *Ancient Inventions*, Ballantine Books, New York.

5. Johnson, Frank H, et. al., 1991, "Safer ATV," *Proceedings of the Passenger Car Meeting and Exposition*, Vol 45, pp.1-12

6. Koon, W. S., 1997, "Reduction, Reconstruction and Optimal Control of Nonholonomic Mechanical Systems with Symmetry (Lagrangian Reduction, Hamiltonian Dynamics)," Ph.D. Dissertation, University of California, Berkeley.

7. Mächler, Philip, "Pemex-BE ," Ecole polytechnique fédérale de Lausanne, IAV 95 (IFIP Intelligent Autonomous Vehicles Conference), Espoo, FL, June 14, 1995

8. Meirovitch, L., 1989, *Dynamics and Control of Structures*, Wiley Interscience, New York.

9. Meirovitch, L., 1970, *Methods of Analytical Dynamics*, McGraw-Hill, New York.

10. Neimark, J. I., and Fufave, N. A., 1972, *Dynamics of Nonholonomic Systems*, American Mathematical Society, Providence, RI.

11. Nayfeh, A. H. and Mook, D. T., 1979, *Nonlinear Oscillations*, Wiley, New York.

12. Politnasky, H., and Pilkey, W. D., 1989, "Suboptimal Feedback Vibration Control of a Beam with a Proof-Mass", *Journal of Guidance Control and Dynamics*, V.12, Sept., pp. 691-97.

13. Reinholtz, C. F., Bay, J., Soper, R. R., Abbott, M. S., and Grove, D. E., 1999, "The Biplanar Bicycle," *Proceedings of the 1999 ASME International Mechanical Engineering Congress and Exposition*, Nashville, TN. Nov. 14-19

14. Slotine, J.-J. E., and Li, W., 1991, *Applied Nonlinear Control*, Prentice Hall, Englewood Cliffs, NJ.

15. Wolovich, W. A., 1994, *Automatic Control Systems: Basic Analysis and Design*, Saunders College Publishing, Fort Worth.

16. Zhou, K., Doyle, J. C., and Glover, K., 1996, *Robust and Optimal Control*, Prentice Hall, New Jersey.

17. Zimmerman, D. C., Inman, D. J., and Horner, G. C., 1984, "Dynamic Characterization and Microprocessor control of the NASA/UVA Proof-Mass Actuator," AIAA Paper 84-1077, May.

PATENTS

1. Barber, G., 1977, "Vehicle, Especially Amusement Vehicle," U.S. Patent 4163567

2. Horn, A., 1991, "Stabilized High Speed Bi-Wheeled Vehicle," U.S. Patent 5181740.

3. James, D. W., 1994, "Three Wheeled Competition Wheelchair Having an Adjustable Center of Mass," U.S. Patent 5480172

4. Morin, D., 1984, "Spherical Rolling Cage for Recreation and Entertainment," U.S. Patent 4579336

5. Namngani, A., 1998, "Vehicle having two axially spaced relatively movable wheels," U.S. Patent 5769441.

6. Salmon, J. R., 1987, "Rowing Type Vehicle," U.S. Patent 4700962.

7. Samsel, F., 1974, "Toy Vehicle," U.S. Patent 3893707

8. Werdner, M., 1986, "Cross-Country Vehicle," U.S. Patent 4779691.

Web Pages

1. http://www.rqriley.com/

Appendix: Listing of 3D Mathematica Code

The following appendix presents the code used to solve the 3D equations of motion and presents the resulting coupled, non-linear set of equations needed to solve the system dynamics. The solutions of these equations are not provided here.

Biplanar Bicycle on a 1-2 Rotated Plane

```
In[1]:= Off[General::spell1];
```

■ NonDimensionalization of Variables and Parameters

```
(* ωc=√(g/r) *)

In[2]:= NonDimRule = {L -> Lc R, d -> s R, m -> Γ mt, M -> (1 - Γ) mt, I -> Σ mt R^2,
          c -> R^2 mt ωc ζ, g -> R ωc^2, U[t] -> R^2 mt ωc^2 / k1 u[t], k2 -> R^2 mt ωc K};
        TimeRule =
         {θ'[t] -> ωc θ'[t], θ''[t] -> ωc^2 θ''[t], ϕ'[t] -> ωc ϕ'[t], ϕ''[t] -> ωc^2 ϕ''[t]};
        ForceRule = {λ1[t] -> Λ1[t] mt R ωc^2, λ2[t] -> Λ2[t] mt R ωc^2,
          λ1'[t] -> D[(Λ1[t] mt R ωc^2), t], λ2'[t] -> D[(Λ2[t] mt R ωc^2), t]};
        InputRule = {θr[t] -> ThetaR, θr'[t] -> dThetaR, θl[t] -> ThetaL, θl'[t] -> dThetaL,
          ϕ[t] -> Phi, ϕ'[t] -> dPhi, βx -> xSlope, βy -> ySlope, Γ -> MR, ωc -> Omega};
```

■ Kinematic Definitions

```
In[3]:= Q[t] = {x[t] + L Sin[ϕ[t]] Cos[α[t]] , y[t] + L Sin[ϕ[t]] Sin[α[t]] , R - L Cos[ϕ[t]]};
        Pright[t] = {x[t] + d Sin[α[t]] , y[t] - d Cos[α[t]] , R};
        Pleft[t] = {x[t] - d Sin[α[t]] , y[t] + d Cos[α[t]] , R};
        G = {g Sin[βx] , -g Sin[βy] Cos[βx] , g Cos[βy] Cos[βx]};
```

■ Energy Definitions

```
In[4]:= T = (1/2 (m D[Q[t], t] . D[Q[t], t] + M D[Pright[t], t] . D[Pright[t], t] +
              M D[Pleft[t], t] . D[Pleft[t], t] + I θr'[t] + I θl'[t]));
```

The potential field is defined by the resulting gravitational field on a plane once rotated through an absolute (not Euler) 1-2 rotation

```
In[5]:= V = (Q[t] . G + Pright[t] . G + Pleft[t] . G);

In[6]:= Ray = (1/2 c ((θr'[t] + ϕ'[t])^2 + (θl'[t] + ϕ'[t])^2));
```

■ Generalized Forces

```
In[7]:= K1 = Kt / Ra;
        K2 = Kt Kb / Ra;
```

```
In[8]:= Qθr[t] = K1 Uar - K2 (θr'[t] + ϕ'[t]) /. NonDimRule /. TimeRule /. ForceRule;
        Qθl[t] = K1 Ual - K2 (θl'[t] + ϕ'[t]) /. NonDimRule /. TimeRule /. ForceRule;
        Qϕ[
          t] = K1 (Uar + Ual) - K2 (θr'[t] + θl'[t] + 2 ϕ'[t]) /. NonDimRule /. TimeRule /. ForceRule;
```

■ Constraint Equation for α

```
In[9]:= αConstraint = {α[t] -> R (θr[t] + θl[t]) / (2 d), α'[t] -> R (θr'[t] + θl'[t]) / (2 d),
          α''[t] -> R (θr''[t] + θl''[t]) / (2 d)};
```

■ Constraint Equations for ONE WHEEL -- See Proof

```
In[10]:= xConstraint = (x'[t] + α'[t] d Cos[α[t]] - R θr'[t] Cos[α[t]]) /. αConstraint;
         yConstraint = y'[t] + α'[t] d Sin[α[t]] - R θr'[t] Sin[α[t]] /. αConstraint;
```

■ Derivatives of Above constraints needed to solve for the λs

```
In[11]:= DxConstraint = D[(xConstraint), t];
         DyConstraint = D[(yConstraint), t];
```

■ Coefficients for Lagrange Multipliers in x and y directions, $\lambda 1$ and $\lambda 2$, respectively

```
In[12]:= θrxMul = (λ1[t] D[(xConstraint), θr[t]] - D[(λ1[t] D[(xConstraint), θr'[t]]), t]) /.
             NonDimRule /. TimeRule /. ForceRule;
         θryMul =
          (λ2[t] D[yConstraint, θr[t]] - D[(λ2[t] D[yConstraint, θr'[t]]), t]) /. NonDimRule /.
            TimeRule /. ForceRule;

In[13]:= θlxMul = (λ1[t] D[xConstraint, θl[t]] - D[(λ1[t] D[xConstraint, θl'[t]]), t]) /.
             NonDimRule /. TimeRule /. ForceRule;
         θlyMul =
          (λ2[t] D[yConstraint, θl[t]] - D[(λ2[t] D[yConstraint, θl'[t]]), t]) /. NonDimRule /.
            TimeRule /. ForceRule;

In[14]:= ϕxMul = λ1[t] D[xConstraint, ϕ[t]] - D[(λ1[t] D[xConstraint, ϕ'[t]]), t] /. NonDimRule /
            TimeRule /. ForceRule;
         ϕyMul = λ2[t] D[yConstraint, ϕ[t]] - D[(λ2[t] D[yConstraint, ϕ'[t]]), t] /. NonDimRule /
            TimeRule /. ForceRule;

In[15]:= xxMul = λ1[t] D[xConstraint, x[t]] - D[(λ1[t] D[xConstraint, x'[t]]), t] /. NonDimRule /
            TimeRule /. ForceRule;
         xyMul = λ2[t] D[yConstraint, x[t]] - D[(λ2[t] D[yConstraint, x'[t]]), t] /. NonDimRule /
            TimeRule /. ForceRule;
```

```
In[16]:= yxMul = λ1[t] D[xConstraint, y[t]] - D[(λ1[t] D[xConstraint, y'[t]]), t] /. NonDimRule /
           TimeRule /. ForceRule;
         yyMul = λ2[t] D[yConstraint, y[t]] - D[(λ2[t] D[yConstraint, y'[t]]), t] /. NonDimRule /
           TimeRule /. ForceRule;
```

■ The Euler-Lagrange equations

```
In[17]:= lagrangian = (T - V) /. αConstraint //. NonDimRule /. TimeRule;

In[18]:= EOM[coord_] :=
          D[D[lagrangian, D[coord, t]], t] - D[lagrangian, coord] + D[Ray, D[coord, t]];
```

■ Equations of Motion, θ_r, θ_l, ϕ, x, y,

```
In[22]:= eqθr = (EOM[θr[t]] - Qθr[t] - θrxMul - θryMul);

In[24]:= eqθl = (EOM[θl[t]] - Qθl[t] - θlxMul - θlyMul);

In[26]:= eqϕ = (EOM[ϕ[t]] - Qϕ[t] - ϕxMul - ϕyMul);

In[28]:= eqx = (EOM[x[t]] - xxMul - xyMul);

In[31]:= eqy = (EOM[y[t]] - yxMul - yyMul);

In[32]:= ddxddyRule = Solve[{(DxConstraint //. NonDimRule //. TimeRule //. ForceRule) == 0,
            (DyConstraint //. NonDimRule //. TimeRule //. ForceRule) == 0}, {x''[t], y''[t]}] //
          Flatten;

In[33]:= LambdaSol = Solve[{(eqx /. ddxddyRule) == 0, (eqy /. ddxddyRule) == 0}, {λ1'[t], λ2'[t]}];
```

Solving the full variational result of the extended Lagrange equation using $q_j = q_R$ yields the following expression which should be set equal to zero.

$$\frac{1}{4\,Ra\,s^2}\Bigg(-4\,Kt\,s^2\,Uar - 2\,Lc\,R^2\,Ra\,s\,\omega c^2\,\cos[\beta x]\,\cos\Big[\frac{\theta 1[t]+\theta r[t]}{2s}\Big]\,\sin[\beta y]\,\sin[\phi[t]] -$$
$$2\,Lc\,R^2\,Ra\,s\,\omega c^2\,\sin[\beta x]\,\sin\Big[\frac{\theta 1[t]+\theta r[t]}{2s}\Big]\,\sin[\phi[t]] +$$
$$2\,mt\,R^2\,Ra\,s\,\omega c^2\,\sin\Big[\frac{\theta 1[t]+\theta r[t]}{2s}\Big]\,A1[t]\,\theta 1'[t] - 2\,mt\,R^2\,Ra\,s\,\omega c^2\,\cos\Big[\frac{\theta 1[t]+\theta r[t]}{2s}\Big]\,A2[t]\,\theta 1'[t] + 4\,Kb\,Kt\,s^2\,\theta r'[t] +$$
$$4\,c\,Ra\,s^2\,\theta r'[t] - 2\,mt\,R^2\,Ra\,s^2\,\omega c^2\,\cos\Big[\frac{\theta 1[t]+\theta r[t]}{2s}\Big]\,A1'[t] - 2\,mt\,R^2\,Ra\,s^2\,\omega c^2\,\sin\Big[\frac{\theta 1[t]+\theta r[t]}{2s}\Big]\,A2'[t] +$$
$$4\,c\,Ra\,s^2\,\phi'[t] + 4\,Kb\,Kt\,s^2\,\omega c\,\phi'[t] - 2\,Lc\,mt\,R\,Ra\,s\,\Gamma\,\cos[\phi[t]]\,\sin\Big[\frac{\theta 1[t]+\theta r[t]}{2s}\Big]\,x'[t]\,\phi'[t] +$$
$$2\,Lc\,mt\,R\,Ra\,s\,\Gamma\,\omega c\,\cos[\phi[t]]\,\sin\Big[\frac{\theta 1[t]+\theta r[t]}{2s}\Big]\,x'[t]\,\phi'[t] +$$
$$2\,Lc\,mt\,R\,Ra\,s\,\Gamma\,\cos\Big[\frac{\theta 1[t]+\theta r[t]}{2s}\Big]\,\cos[\phi[t]]\,y'[t]\,\phi'[t] -$$
$$2\,Lc\,mt\,R\,Ra\,s\,\Gamma\,\omega c\,\cos\Big[\frac{\theta 1[t]+\theta r[t]}{2s}\Big]\,\cos[\phi[t]]\,y'[t]\,\phi'[t] +$$
$$2\,Lc^2\,mt\,R^2\,Ra\,\Gamma\,\cos\Big[\frac{\theta 1[t]+\theta r[t]}{2s}\Big]^2\,\cos[\phi[t]]\,\sin[\phi[t]]\,\theta 1'[t]\,\phi'[t] +$$
$$2\,Lc^2\,mt\,R^2\,Ra\,\Gamma\,\cos[\phi[t]]\,\sin\Big[\frac{\theta 1[t]+\theta r[t]}{2s}\Big]^2\,\sin[\phi[t]]\,\theta 1'[t]\,\phi'[t] +$$
$$2\,Lc^2\,mt\,R^2\,Ra\,\Gamma\,\cos\Big[\frac{\theta 1[t]+\theta r[t]}{2s}\Big]^2\,\cos[\phi[t]]\,\sin[\phi[t]]\,\theta r'[t]\,\phi'[t] + 2\,Lc^2\,mt\,R^2\,Ra\,\Gamma\,\cos[\phi[t]]$$
$$\sin\Big[\frac{\theta 1[t]+\theta r[t]}{2s}\Big]^2\,\sin[\phi[t]]\,\theta r'[t]\,\phi'[t] - 2\,Lc\,mt\,R\,Ra\,s\,\Gamma\,\sin\Big[\frac{\theta 1[t]+\theta r[t]}{2s}\Big]\,\sin[\phi[t]]\,x''[t] +$$
$$2\,Lc\,mt\,R\,Ra\,s\,\Gamma\,\cos\Big[\frac{\theta 1[t]+\theta r[t]}{2s}\Big]\,\sin[\phi[t]]\,y''[t] + 2\,mt\,R^2\,Ra\,s^2\,\cos\Big[\frac{\theta 1[t]+\theta r[t]}{2s}\Big]^2\,\theta 1''[t] -$$
$$2\,mt\,R^2\,Ra\,s^2\,\Gamma\,\cos\Big[\frac{\theta 1[t]+\theta r[t]}{2s}\Big]^2\,\theta 1''[t] + 2\,mt\,R^2\,Ra\,s^2\,\sin\Big[\frac{\theta 1[t]+\theta r[t]}{2s}\Big]^2\,\theta 1''[t] -$$
$$2\,mt\,R^2\,Ra\,s^2\,\Gamma\,\sin\Big[\frac{\theta 1[t]+\theta r[t]}{2s}\Big]^2\,\theta 1''[t] + Lc^2\,mt\,R^2\,Ra\,\Gamma\,\cos\Big[\frac{\theta 1[t]+\theta r[t]}{2s}\Big]^2\,\sin[\phi[t]]^2\,\theta 1''[t] +$$
$$Lc^2\,mt\,R^2\,Ra\,\Gamma\,\sin\Big[\frac{\theta 1[t]+\theta r[t]}{2s}\Big]^2\,\sin[\phi[t]]^2\,\theta 1''[t] + 2\,mt\,R^2\,Ra\,s^2\,\cos\Big[\frac{\theta 1[t]+\theta r[t]}{2s}\Big]^2\,\theta r''[t] -$$
$$2\,mt\,R^2\,Ra\,s^2\,\Gamma\,\cos\Big[\frac{\theta 1[t]+\theta r[t]}{2s}\Big]^2\,\theta r''[t] + 2\,mt\,R^2\,Ra\,s^2\,\sin\Big[\frac{\theta 1[t]+\theta r[t]}{2s}\Big]^2\,\theta r''[t] -$$
$$2\,mt\,R^2\,Ra\,s^2\,\Gamma\,\sin\Big[\frac{\theta 1[t]+\theta r[t]}{2s}\Big]^2\,\theta r''[t] + Lc^2\,mt\,R^2\,Ra\,\Gamma\,\cos\Big[\frac{\theta 1[t]+\theta r[t]}{2s}\Big]^2\,\sin[\phi[t]]^2\,\theta r''[t] +$$
$$Lc^2\,mt\,R^2\,Ra\,\Gamma\,\sin\Big[\frac{\theta 1[t]+\theta r[t]}{2s}\Big]^2\,\sin[\phi[t]]^2\,\theta r''[t]\Bigg)$$

Solving the full variational result of the extended Lagrange equation using $q_j = q_L$ yields the following expression which should be set equal to zero.

$$\frac{1}{4\,Ra\,s^2}\Big(-4\,Kt\,s^2\,Ual - 2\,Lc\,R^2\,Ra\,s\,\omega c^2\,Cos[\beta x]\,Cos\Big[\frac{\theta l[t]+\theta r[t]}{2\,s}\Big]\,Sin[\beta y]\,Sin[\phi[t]] -$$
$$2\,Lc\,R^2\,Ra\,s\,\omega c^2\,Sin[\beta x]\,Sin\Big[\frac{\theta l[t]+\theta r[t]}{2\,s}\Big]\,Sin[\phi[t]] -$$
$$2\,mt\,R^2\,Ra\,s\,\omega c^2\,Sin\Big[\frac{\theta l[t]+\theta r[t]}{2\,s}\Big]\,A1[t]\,\theta r'[t] +$$
$$2\,mt\,R^2\,Ra\,s\,\omega c^2\,Cos\Big[\frac{\theta l[t]+\theta r[t]}{2\,s}\Big]\,A2[t]\,\theta r'[t] +$$
$$2\,mt\,R^2\,Ra\,s^2\,\omega c^2\,Cos\Big[\frac{\theta l[t]+\theta r[t]}{2\,s}\Big]\,A1'[t] +$$
$$2\,mt\,R^2\,Ra\,s^2\,\omega c^2\,Sin\Big[\frac{\theta l[t]+\theta r[t]}{2\,s}\Big]\,A2'[t] + 4\,c\,Ra\,s^2\,\phi'[t] +$$
$$4\,Kb\,Kt\,s^2\,\omega c\,\phi'[t] - 2\,Lc\,mt\,R\,Ra\,s\,\Gamma\,Cos[\phi[t]]\,Sin\Big[\frac{\theta l[t]+\theta r[t]}{2\,s}\Big]\,x'[t]\,\phi'[t] +$$
$$2\,Lc\,mt\,R\,Ra\,s\,\Gamma\,\omega c\,Cos[\phi[t]]\,Sin\Big[\frac{\theta l[t]+\theta r[t]}{2\,s}\Big]\,x'[t]\,\phi'[t] +$$
$$2\,Lc\,mt\,R\,Ra\,s\,\Gamma\,Cos\Big[\frac{\theta l[t]+\theta r[t]}{2\,s}\Big]\,Cos[\phi[t]]\,y'[t]\,\phi'[t] -$$
$$2\,Lc\,mt\,R\,Ra\,s\,\Gamma\,\omega c\,Cos\Big[\frac{\theta l[t]+\theta r[t]}{2\,s}\Big]\,Cos[\phi[t]]\,y'[t]\,\phi'[t] +$$
$$2\,Lc^2\,mt\,R^2\,Ra\,\Gamma\,Cos\Big[\frac{\theta l[t]+\theta r[t]}{2\,s}\Big]^2\,Cos[\phi[t]]\,Sin[\phi[t]]\,\theta r'[t]\,\phi'[t] +$$
$$2\,Lc^2\,mt\,R^2\,Ra\,\Gamma\,Cos[\phi[t]]\,Sin\Big[\frac{\theta l[t]+\theta r[t]}{2\,s}\Big]^2\,Sin[\phi[t]]\,\theta r'[t]\,\phi'[t] +$$
$$\theta l'[t]\,(4\,(Kb\,Kt + c\,Ra)\,s^2 + Lc^2\,mt\,R^2\,Ra\,\Gamma\,Sin[2\,\phi[t]]\,\phi'[t]) -$$
$$2\,Lc\,mt\,R\,Ra\,s\,\Gamma\,Sin\Big[\frac{\theta l[t]+\theta r[t]}{2\,s}\Big]\,Sin[\phi[t]]\,x''[t] +$$
$$2\,Lc\,mt\,R\,Ra\,s\,\Gamma\,Cos\Big[\frac{\theta l[t]+\theta r[t]}{2\,s}\Big]\,Sin[\phi[t]]\,y''[t] +$$
$$2\,mt\,R^2\,Ra\,s^2\,Cos\Big[\frac{\theta l[t]+\theta r[t]}{2\,s}\Big]^2\,\theta l''[t] - 2\,mt\,R^2\,Ra\,s^2\,\Gamma\,Cos\Big[\frac{\theta l[t]+\theta r[t]}{2\,s}\Big]^2\,\theta l''[t] +$$
$$2\,mt\,R^2\,Ra\,s^2\,Sin\Big[\frac{\theta l[t]+\theta r[t]}{2\,s}\Big]^2\,\theta l''[t] - 2\,mt\,R^2\,Ra\,s^2\,\Gamma\,Sin\Big[\frac{\theta l[t]+\theta r[t]}{2\,s}\Big]^2\,\theta l''[t] +$$
$$Lc^2\,mt\,R^2\,Ra\,\Gamma\,Cos\Big[\frac{\theta l[t]+\theta r[t]}{2\,s}\Big]^2\,Sin[\phi[t]]^2\,\theta l''[t] +$$
$$Lc^2\,mt\,R^2\,Ra\,\Gamma\,Sin\Big[\frac{\theta l[t]+\theta r[t]}{2\,s}\Big]^2\,Sin[\phi[t]]^2\,\theta l''[t] +$$
$$2\,mt\,R^2\,Ra\,s^2\,Cos\Big[\frac{\theta l[t]+\theta r[t]}{2\,s}\Big]^2\,\theta r''[t] - 2\,mt\,R^2\,Ra\,s^2\,\Gamma\,Cos\Big[\frac{\theta l[t]+\theta r[t]}{2\,s}\Big]^2\,\theta r''[t] +$$
$$2\,mt\,R^2\,Ra\,s^2\,Sin\Big[\frac{\theta l[t]+\theta r[t]}{2\,s}\Big]^2\,\theta r''[t] - 2\,mt\,R^2\,Ra\,s^2\,\Gamma\,Sin\Big[\frac{\theta l[t]+\theta r[t]}{2\,s}\Big]^2\,\theta r''[t] +$$
$$Lc^2\,mt\,R^2\,Ra\,\Gamma\,Cos\Big[\frac{\theta l[t]+\theta r[t]}{2\,s}\Big]^2\,Sin[\phi[t]]^2\,\theta r''[t] +$$
$$Lc^2\,mt\,R^2\,Ra\,\Gamma\,Sin\Big[\frac{\theta l[t]+\theta r[t]}{2\,s}\Big]^2\,Sin[\phi[t]]^2\,\theta r''[t]\Big)$$

Solving the full variational result of the extended Lagrange equation using $q_j = f$ yields the following expression which should be set equal to zero.

$$
\begin{aligned}
&\frac{1}{4\,Ra\,s^2}\Big(-\frac{1}{2}\,Lc^2\,mt\,R^2\,Ra\,\Gamma\,\sin[2\,\phi[t]]\,\theta l'[t]^2 + \\
&\quad 2\,s\Big(2\,Kb\,Kt\,s + 2\,c\,Ra\,s + Lc\,mt\,R\,Ra\,\Gamma\cos[\phi[t]]\sin\Big[\frac{\theta l[t]+\theta r[t]}{2\,s}\Big]\,x'[t] - \\
&\qquad Lc\,mt\,R\,Ra\,\Gamma\,\omega c\cos[\phi[t]]\sin\Big[\frac{\theta l[t]+\theta r[t]}{2\,s}\Big]\,x'[t] - \\
&\qquad Lc\,mt\,R\,Ra\,\Gamma\cos\Big[\frac{\theta l[t]+\theta r[t]}{2\,s}\Big]\cos[\phi[t]]\,y'[t] + \\
&\qquad Lc\,mt\,R\,Ra\,\Gamma\,\omega c\cos\Big[\frac{\theta l[t]+\theta r[t]}{2\,s}\Big]\cos[\phi[t]]\,y'[t]\Big)\,\theta r'[t] - \\
&\quad \frac{1}{2}\,Lc^2\,mt\,R^2\,Ra\,\Gamma\,\sin[2\,\phi[t]]\,\theta r'[t]^2 + \\
&\quad 2\,\theta l'[t]\Big(2\,Kb\,Kt\,s^2 + 2\,c\,Ra\,s^2 - Lc\,mt\,R\,Ra\,s\,\Gamma\,(-1+\omega c)\cos[\phi[t]]\sin\Big[\frac{\theta l[t]+\theta r[t]}{2\,s}\Big]\,x'[t] - \\
&\qquad Lc\,mt\,R\,Ra\,s\,\Gamma\cos\Big[\frac{\theta l[t]+\theta r[t]}{2\,s}\Big]\cos[\phi[t]]\,y'[t] + \\
&\qquad Lc\,mt\,R\,Ra\,s\,\Gamma\,\omega c\cos\Big[\frac{\theta l[t]+\theta r[t]}{2\,s}\Big]\cos[\phi[t]]\,y'[t] - \\
&\qquad Lc^2\,mt\,R^2\,Ra\,\Gamma\cos\Big[\frac{\theta l[t]+\theta r[t]}{2\,s}\Big]^2\cos[\phi[t]]\sin[\phi[t]]\,\theta r'[t] - \\
&\qquad Lc^2\,mt\,R^2\,Ra\,\Gamma\cos[\phi[t]]\sin\Big[\frac{\theta l[t]+\theta r[t]}{2\,s}\Big]^2\sin[\phi[t]]\,\theta r'[t]\Big) + \\
&\quad 2\,s^2\Big(-2\,Kt\,Ual - 2\,Kt\,Uar + 2\,Lc\,R^2\,Ra\,\omega c^2\cos\Big[\frac{\theta l[t]+\theta r[t]}{2\,s}\Big]\cos[\phi[t]]\sin[\beta x] - \\
&\qquad 2\,Lc\,R^2\,Ra\,\omega c^2\cos[\beta x]\cos[\phi[t]]\sin[\beta y]\sin\Big[\frac{\theta l[t]+\theta r[t]}{2\,s}\Big] + \\
&\qquad 2\,Lc\,R^2\,Ra\,\omega c^2\cos[\beta x]\cos[\beta y]\sin[\phi[t]] + 4\,c\,Ra\,\phi'[t] + 4\,Kb\,Kt\,\omega c\,\phi'[t] - 2\,Lc^2\,mt\,R^2\,Ra\,\Gamma \\
&\qquad \omega c^2\cos\Big[\frac{\theta l[t]+\theta r[t]}{2\,s}\Big]^2\cos[\phi[t]]\sin[\phi[t]]\,\phi'[t]^2 - 2\,Lc^2\,mt\,R^2\,Ra\,\Gamma\,\omega c^2\cos[\phi[t]] \\
&\qquad \sin\Big[\frac{\theta l[t]+\theta r[t]}{2\,s}\Big]^2\sin[\phi[t]]\,\phi'[t]^2 + Lc^2\,mt\,R^2\,Ra\,\Gamma\,\omega c^2\sin[2\,\phi[t]]\,\phi'[t]^2 + \\
&\qquad 2\,Lc\,mt\,R\,Ra\,\Gamma\,\omega c\cos\Big[\frac{\theta l[t]+\theta r[t]}{2\,s}\Big]\cos[\phi[t]]\,x''[t] + \\
&\qquad 2\,Lc\,mt\,R\,Ra\,\Gamma\,\omega c\cos[\phi[t]]\sin\Big[\frac{\theta l[t]+\theta r[t]}{2\,s}\Big]\,y''[t] + \\
&\qquad 2\,Lc^2\,mt\,R^2\,Ra\,\Gamma\,\omega c^2\cos\Big[\frac{\theta l[t]+\theta r[t]}{2\,s}\Big]^2\cos[\phi[t]]^2\,\phi''[t] + \\
&\qquad 2\,Lc^2\,mt\,R^2\,Ra\,\Gamma\,\omega c^2\cos[\phi[t]]^2\sin\Big[\frac{\theta l[t]+\theta r[t]}{2\,s}\Big]^2\phi''[t] + \\
&\qquad 2\,Lc^2\,mt\,R^2\,Ra\,\Gamma\,\omega c^2\sin[\phi[t]]^2\,\phi''[t]\Big)\Big)
\end{aligned}
$$

Solving the full variational result of the extended Lagrange equation using $q_j = x$ yields the following expression which should be set equal to zero.

$$
\begin{aligned}
&-\frac{1}{4\,s^2}\Big(\mathrm{Lc\,mt\,R\,\Gamma}\,\mathrm{Cos}\Big[\frac{\theta l[t]+\theta r[t]}{2\,s}\Big]\,\mathrm{Sin}[\phi[t]]\,\theta l'[t]^2+\\
&\quad \mathrm{Lc\,mt\,R\,\Gamma}\,\mathrm{Cos}\Big[\frac{\theta l[t]+\theta r[t]}{2\,s}\Big]\,\mathrm{Sin}[\phi[t]]\,\theta r'[t]^2+\\
&\quad 2\,\mathrm{Lc\,mt\,R\,s\,\Gamma}\,(1+\omega c)\,\mathrm{Cos}[\phi[t]]\,\mathrm{Sin}\Big[\frac{\theta l[t]+\theta r[t]}{2\,s}\Big]\,\theta r'[t]\,\phi'[t]+\\
&\quad 2\,\mathrm{Lc\,mt\,R\,\Gamma}\,\theta l'[t]\Big(\mathrm{Cos}\Big[\frac{\theta l[t]+\theta r[t]}{2\,s}\Big]\,\mathrm{Sin}[\phi[t]]\,\theta r'[t]+\\
&\qquad s\,(1+\omega c)\,\mathrm{Cos}[\phi[t]]\,\mathrm{Sin}\Big[\frac{\theta l[t]+\theta r[t]}{2\,s}\Big]\,\phi'[t]\Big)+\\
&\quad 2\,s\Big(-6\,R\,s\,\omega c^2\,\mathrm{Sin}[\beta x]-\\
&\qquad 2\,\mathrm{mt\,R\,s}\,\omega c^2\,A1'[t]+2\,\mathrm{Lc\,mt\,R\,s\,\Gamma}\,\omega c\,\mathrm{Cos}\Big[\frac{\theta l[t]+\theta r[t]}{2\,s}\Big]\,\mathrm{Sin}[\phi[t]]\,\phi'[t]^2-\\
&\qquad 4\,\mathrm{mt\,s}\,x''[t]+2\,\mathrm{mt\,s\,\Gamma}\,x''[t]+\mathrm{Lc\,mt\,R\,\Gamma}\,\mathrm{Sin}\Big[\frac{\theta l[t]+\theta r[t]}{2\,s}\Big]\,\mathrm{Sin}[\phi[t]]\,\theta l''[t]+\\
&\qquad \mathrm{Lc\,mt\,R\,\Gamma}\,\mathrm{Sin}\Big[\frac{\theta l[t]+\theta r[t]}{2\,s}\Big]\,\mathrm{Sin}[\phi[t]]\,\theta r''[t]-\\
&\qquad 2\,\mathrm{Lc\,mt\,R\,s\,\Gamma}\,\omega c\,\mathrm{Cos}\Big[\frac{\theta l[t]+\theta r[t]}{2\,s}\Big]\,\mathrm{Cos}[\phi[t]]\,\phi''[t]\Big)\Big)
\end{aligned}
$$

Solving the full variational result of the extended Lagrange equation using $q_j = y$ yields the following expression which should be set equal to zero.

$$
\begin{aligned}
&\frac{1}{4\,s^2}\Big(-\mathrm{Lc\,mt\,R\,\Gamma}\,\mathrm{Sin}\Big[\frac{\theta l[t]+\theta r[t]}{2\,s}\Big]\,\mathrm{Sin}[\phi[t]]\,\theta l'[t]^2-\\
&\quad \mathrm{Lc\,mt\,R\,\Gamma}\,\mathrm{Sin}\Big[\frac{\theta l[t]+\theta r[t]}{2\,s}\Big]\,\mathrm{Sin}[\phi[t]]\,\theta r'[t]^2+\\
&\quad 2\,\mathrm{Lc\,mt\,R\,s\,\Gamma}\,(1+\omega c)\,\mathrm{Cos}\Big[\frac{\theta l[t]+\theta r[t]}{2\,s}\Big]\,\mathrm{Cos}[\phi[t]]\,\theta r'[t]\,\phi'[t]+\\
&\quad 2\,\mathrm{Lc\,mt\,R\,\Gamma}\,\theta l'[t]\Big(-\mathrm{Sin}\Big[\frac{\theta l[t]+\theta r[t]}{2\,s}\Big]\,\mathrm{Sin}[\phi[t]]\,\theta r'[t]+\\
&\qquad s\,(1+\omega c)\,\mathrm{Cos}\Big[\frac{\theta l[t]+\theta r[t]}{2\,s}\Big]\,\mathrm{Cos}[\phi[t]]\,\phi'[t]\Big)+\\
&\quad 2\,s\Big(-6\,R\,s\,\omega c^2\,\mathrm{Cos}[\beta x]\,\mathrm{Sin}[\beta y]+\\
&\qquad 2\,\mathrm{mt\,R\,s}\,\omega c^2\,A2'[t]-2\,\mathrm{Lc\,mt\,R\,s\,\Gamma}\,\omega c\,\mathrm{Sin}\Big[\frac{\theta l[t]+\theta r[t]}{2\,s}\Big]\,\mathrm{Sin}[\phi[t]]\,\phi'[t]^2+\\
&\qquad 4\,\mathrm{mt\,s}\,y''[t]-2\,\mathrm{mt\,s\,\Gamma}\,y''[t]+\mathrm{Lc\,mt\,R\,\Gamma}\,\mathrm{Cos}\Big[\frac{\theta l[t]+\theta r[t]}{2\,s}\Big]\,\mathrm{Sin}[\phi[t]]\,\theta l''[t]+\\
&\qquad \mathrm{Lc\,mt\,R\,\Gamma}\,\mathrm{Cos}\Big[\frac{\theta l[t]+\theta r[t]}{2\,s}\Big]\,\mathrm{Sin}[\phi[t]]\,\theta r''[t]+\\
&\qquad 2\,\mathrm{Lc\,mt\,R\,s\,\Gamma}\,\omega c\,\mathrm{Cos}[\phi[t]]\,\mathrm{Sin}\Big[\frac{\theta l[t]+\theta r[t]}{2\,s}\Big]\,\phi''[t]\Big)\Big)
\end{aligned}
$$

Solving for the first derivative of the the multipliers yields the following two expressions:

$$
\begin{aligned}
\lambda 1'[t] \to -\frac{1}{mt\, R\, \omega c^2}\Bigg(& 3\, R\, \omega c^2\, \sin[\beta x] + \frac{1}{2}\Bigg(2\, mt\, (1-\Gamma)\Bigg(\frac{R \sin\left[\frac{\theta l[t]+\theta r[t]}{2s}\right](\theta l'[t]+\theta r'[t])^2}{4s} - \\
& \frac{1}{2} R \cos\left[\frac{\theta l[t]+\theta r[t]}{2s}\right](\theta l''[t]+\theta r''[t]) - \\
& \frac{1}{4s}\Bigg(-R \sin\left[\frac{\theta l[t]+\theta r[t]}{2s}\right]\theta l'[t]^2 + R \sin\left[\frac{\theta l[t]+\theta r[t]}{2s}\right]\theta r'[t]^2 + \\
& 2\, R\, s \cos\left[\frac{\theta l[t]+\theta r[t]}{2s}\right]\theta l''[t] - 2\, R\, s \cos\left[\frac{\theta l[t]+\theta r[t]}{2s}\right]\theta r''[t]\Bigg)\Bigg) + \\
& 2\, mt\, (1-\Gamma)\Bigg(-\frac{R \sin\left[\frac{\theta l[t]+\theta r[t]}{2s}\right](\theta l'[t]+\theta r'[t])^2}{4s} + \\
& \frac{1}{2} R \cos\left[\frac{\theta l[t]+\theta r[t]}{2s}\right](\theta l''[t]+\theta r''[t]) - \\
& \frac{1}{4s}\Bigg(-R \sin\left[\frac{\theta l[t]+\theta r[t]}{2s}\right]\theta l'[t]^2 + R \sin\left[\frac{\theta l[t]+\theta r[t]}{2s}\right]\theta r'[t]^2 + \\
& 2\, R\, s \cos\left[\frac{\theta l[t]+\theta r[t]}{2s}\right]\theta l''[t] - 2\, R\, s \cos\left[\frac{\theta l[t]+\theta r[t]}{2s}\right]\theta r''[t]\Bigg)\Bigg) + \\
& 2\, mt\, \Gamma\Bigg(-\frac{Lc\, R \cos\left[\frac{\theta l[t]+\theta r[t]}{2s}\right]\sin[\phi[t]](\theta l'[t]+\theta r'[t])^2}{4s^2} - \\
& \frac{Lc\, R \cos[\phi[t]] \sin\left[\frac{\theta l[t]+\theta r[t]}{2s}\right](\theta l'[t]+\theta r'[t])\,\phi'[t]}{2s} - \\
& \frac{Lc\, R\, \omega c \cos[\phi[t]] \sin\left[\frac{\theta l[t]+\theta r[t]}{2s}\right](\theta l'[t]+\theta r'[t])\,\phi'[t]}{2s} - \\
& Lc\, R\, \omega c \cos\left[\frac{\theta l[t]+\theta r[t]}{2s}\right]\sin[\phi[t]]\,\phi'[t]^2 - \\
& \frac{Lc\, R \sin\left[\frac{\theta l[t]+\theta r[t]}{2s}\right]\sin[\phi[t]](\theta l''[t]+\theta r''[t])}{2s} - \\
& \frac{1}{4s}\Bigg(-R \sin\left[\frac{\theta l[t]+\theta r[t]}{2s}\right]\theta l'[t]^2 + R \sin\left[\frac{\theta l[t]+\theta r[t]}{2s}\right]\theta r'[t]^2 + \\
& 2\, R\, s \cos\left[\frac{\theta l[t]+\theta r[t]}{2s}\right]\theta l''[t] - 2\, R\, s \cos\left[\frac{\theta l[t]+\theta r[t]}{2s}\right]\theta r''[t]\Bigg) + \\
& Lc\, R\, \omega c \cos\left[\frac{\theta l[t]+\theta r[t]}{2s}\right]\cos[\phi[t]]\,\phi''[t]\Bigg)\Bigg)\Bigg)
\end{aligned}
$$

$$
\begin{aligned}
A2'[t] \to & -\frac{1}{mt\, R\, \omega c^2} \\
& \left(-3\, R\, \omega c^2 \cos[\beta x] \sin[\beta y] + \frac{1}{2}\left(2\, mt\, (1-\Gamma)\left(-\frac{R \cos\left[\frac{\theta l[t]+\theta r[t]}{2s}\right](\theta l'[t]+\theta r'[t])^2}{4s} - \right.\right.\right. \\
& \quad \frac{1}{2} R \sin\left[\frac{\theta l[t]+\theta r[t]}{2s}\right](\theta l''[t]+\theta r''[t]) - \\
& \quad \frac{1}{4s}\left(R \cos\left[\frac{\theta l[t]+\theta r[t]}{2s}\right]\theta l'[t]^2 - R \cos\left[\frac{\theta l[t]+\theta r[t]}{2s}\right]\theta r'[t]^2 + \right. \\
& \quad\quad \left.\left.2\, R\, s \sin\left[\frac{\theta l[t]+\theta r[t]}{2s}\right]\theta l''[t] - 2\, R\, s \sin\left[\frac{\theta l[t]+\theta r[t]}{2s}\right]\theta r''[t]\right)\right) + \\
& \quad 2\, mt\, (1-\Gamma)\left(\frac{R \cos\left[\frac{\theta l[t]+\theta r[t]}{2s}\right](\theta l'[t]+\theta r'[t])^2}{4s} + \right. \\
& \quad \frac{1}{2} R \sin\left[\frac{\theta l[t]+\theta r[t]}{2s}\right](\theta l''[t]+\theta r''[t]) - \\
& \quad \frac{1}{4s}\left(R \cos\left[\frac{\theta l[t]+\theta r[t]}{2s}\right]\theta l'[t]^2 - R \cos\left[\frac{\theta l[t]+\theta r[t]}{2s}\right]\theta r'[t]^2 + \right. \\
& \quad\quad \left.\left.2\, R\, s \sin\left[\frac{\theta l[t]+\theta r[t]}{2s}\right]\theta l''[t] - 2\, R\, s \sin\left[\frac{\theta l[t]+\theta r[t]}{2s}\right]\theta r''[t]\right)\right) + \\
& \quad 2\, mt\, \Gamma\left(-\frac{Lc\, R \sin\left[\frac{\theta l[t]+\theta r[t]}{2s}\right]\sin[\phi[t]](\theta l'[t]+\theta r'[t])^2}{4s^2} + \right. \\
& \quad \frac{Lc\, R \cos\left[\frac{\theta l[t]+\theta r[t]}{2s}\right]\cos[\phi[t]](\theta l'[t]+\theta r'[t])\,\phi'[t]}{2s} + \\
& \quad \frac{Lc\, R\, \omega c \cos\left[\frac{\theta l[t]+\theta r[t]}{2s}\right]\cos[\phi[t]](\theta l'[t]+\theta r'[t])\,\phi'[t]}{2s} - \\
& \quad Lc\, R\, \omega c \sin\left[\frac{\theta l[t]+\theta r[t]}{2s}\right]\sin[\phi[t]]\,\phi'[t]^2 + \\
& \quad \frac{Lc\, R \cos\left[\frac{\theta l[t]+\theta r[t]}{2s}\right]\sin[\phi[t]](\theta l''[t]+\theta r''[t])}{2s} - \\
& \quad \frac{1}{4s}\left(R \cos\left[\frac{\theta l[t]+\theta r[t]}{2s}\right]\theta l'[t]^2 - R \cos\left[\frac{\theta l[t]+\theta r[t]}{2s}\right]\theta r'[t]^2 + \right. \\
& \quad\quad \left.2\, R\, s \sin\left[\frac{\theta l[t]+\theta r[t]}{2s}\right]\theta l''[t] - 2\, R\, s \sin\left[\frac{\theta l[t]+\theta r[t]}{2s}\right]\theta r''[t]\right) + \\
& \quad Lc\, R\, \omega c \cos[\phi[t]] \sin\left[\frac{\theta l[t]+\theta r[t]}{2s}\right]\phi''[t]\Big)\Big)\Big)
\end{aligned}
$$

Vita

Michael S. Abbott was born on February 1, 1974 in Lynchburg Virginia but spent the majority of his childhood in the suburbs of Charlottesville, Virginia. He earned his Bachelor of Science degree in Mechanical Engineering from Virginia Tech in May 1996. He accepted employment with the United States Navy as a civil service engineer at the Naval Air Warfare Center – Aircraft Division located in Patuxent River Maryland. During his tenure with the Navy he did work in both Crew Systems Crashworthiness and in Utility Actuation Subsystems divisions. After two years of simultaneous full-time employment and graduate work with the University of Maryland, College Park, he made the decision to return to Blacksburg to work full-time on his Masters Degree in Mechanical Engineering. He will be beginning his post-graduate career with Key Technologies, a small consulting firm in Baltimore Maryland.